Threshold collision induced dissociation of pyrene cluster cations

Sébastien Zamith, Jean-Marc L'Hermite, Léo Dontot, Linjie Zheng, Mathias Rapacioli, Fernand Spiegelman, Christine Joblin

The Journal of Chemical Physics

Threshold Collision Induced Dissociation of Pyrene Cluster Cations

Sébastien Zamith,[1, a)] Jean-Marc L'Hermite,[1] Léo Dontot,[2] Linjie Zheng,[2] Mathias Rapacioli,[2] Fernand Spiegelman,[2] and Christine Joblin[3]

[1)] *Laboratoire Collision Agrégats Réactivité (LCAR/IRSAMC), UMR5589, Université de Toulouse (UPS) and CNRS, 118 Route de Narbonne, F-31062 Toulouse, France*

[2)] *Laboratoire de Chimie et Physique Quantique (LCPQ/IRSAMC), UMR5626, Université de Toulouse (UPS) and CNRS, 118 Route de Narbonne, F-31062 Toulouse, France*

[3)] *Institut de Recherche en Astrophysique et Planétologie (IRAP), UMR5277, Université de Toulouse (UPS) and CNRS, 9 avenue du Colonel Roche, F-31028 Toulouse, France*

(Dated: 17 July 2020)

We report threshold collision induced dissociation experiments on cationic pyrene clusters, for sizes n=2 to 6. Fragmentation cross-sections were recorded as a function of the collision energy and analyzed with a statistical model. This model can account for the dissociation cascades and provides values for the dissociation energies. These values, of the order of 0.7 to 1 eV, are in excellent agreement with those previously derived from thermal evaporation. They confirm the charge resonance stability enhancement predicted by theoretical calculations. In addition, a remarkable agreement is obtained with theoretical predictions for the two smaller sizes n=2 and 3. For the larger sizes, the agreement remains good, although the theoretical values obtained for the most stable structures are systematically higher by 0.2 eV. This offset could be attributed to approximations in the calculations. Still, there is indication in the results of an incomplete description of the role of isomerization and/or direct dissociation upon collisions. Finally, by-product clusters containing dehydrogenated species are found to dissociate at energies comparable to the non-dehydrogenated ones, which shows no evidence for covalent bonds within the clusters.

[a)] Electronic mail: sebastien.zamith@irsamc.ups-tlse.fr

I. INTRODUCTION

Clusters of Polycyclic Aromatic Hydrocarbons (PAH) have been the topic of several experimental and theoretical investigations in various scientific fields, such as astrophysics, environmental science, combustion science or the search for new organic solar cell devices.

The presence of PAHs in the interstellar medium was proposed in the mid-eighties[1,2]. PAH clusters are likely connected to the evolution of the interstellar PAH population[3,4]. They might be the precursors of free PAHs upon exposure to UV photons in photo-dissociation regions[5] and could play a role in interstellar PAH growth[6–8]. Cationic PAH clusters are expected to be abundant in photo-dissociation regions[9,10] since the ionization energy of the clusters is lower than that of isolated PAHs and decreases with cluster size[11,12] leading to the efficient formation of cationic clusters. In addition, these species are expected to survive longer than their neutral counterparts due to higher dissociation energies, as predicted by calculations[11].

In order to build astrophysical models describing the evolution of the interstellar PAH population, it is important to address the stability of PAH clusters in these environments[9]. The first experimental data were obtained by Schmidt *et al.*[13]. The authors studied the dissociation of clusters of coronene ($C_{24}H_{12}$) after thermalization by a helium bath and interaction with a UV laser. They concluded that the observed dissociation is consistent with an evaporative ensemble and proceeds by the sequential loss of coronene units until the evaporation of the whole cluster or a drop of the temperature of the evaporating cluster below a critical temperature value. These experimental results were successfully described by modeling of the statistical evaporation rate and this model was extended to the case of clusters made of larger PAHs of potential astrophysical interest[10]. Johansson *et al.*[14] have shown that a simple monomer evaporation model is also valid to describe the dissociation of PAH clusters following high-energy collisions with He^{2+} ions.

PAHs from natural and human sources are also found in the atmosphere, known to present a highly toxic character. Thus, understanding the evolution of PAH clusters, eventually incorporating water molecules, is relevant for environmental/atmospheric sciences[15–22]. The role of PAH clusters in the process of soot nucleation is a major topic in the context of combustion, and leads to consider the competition between clustering, evaporation and oligomerization[23–34]. Finally, PAH stacks provide possible compounds to define new organic

solar cell junctions[35–37].

For all these topics there is a need for a better knowledge of the fundamental properties of PAH clusters. Key quantities are the dissociation energies and their evolution with PAH species, cluster size and charge.

In a previous experimental investigation, we have reported the thermal stability of cationic pyrene clusters[38]. Pyrene, $C_{16}H_{10}$, is a planar PAH molecule consisting in the compact arrangement of four fused benzene rings. Temperature dependent breakdown curves of mass selected clusters were measured and we used Phase Space Theory (PST) to calculate evaporation rates and reproduce the experimental results. For each cluster size, there was only one free parameter left in the PST calculations, namely the dissociation energy. For n up to 6, all other parameters (harmonic frequencies, moments of inertia) entering the PST calculations were deduced from recent calculations using Density Functional based Tight Binding coupled with a Configuration Interaction scheme (DFTB-CI) and involving global structural search[39]. The DFTB-CI method[40] is designed to circumvent self-interaction and ill-defined electron-delocalization in cationic molecular clusters and correctly describe charge resonance. For larger sizes, these parameters were extrapolated. We could thus obtain experimental determinations of the dissociation energies of pyrene clusters from sizes n=3 to n=40. The experimental values were found to be fairly consistent with the theoretical DFTB-CI values of Dontot *et al.* although lower by typically 0.2 eV. In addition only a lower limit could be obtained experimentally for the dimer since no evaporation was observed for this ion even at the highest reachable temperature in the experiment.

In this work, we complement our previous experimental investigation of the stability of cationic pyrene clusters by using the Threshold Collision Induced Dissociation (TCID)[41] technique. Using TCID, we are able to characterize the stability of small cationic pyrene clusters in the range n=2-6 and compare the new results with those obtained in the previous work using thermal fragmentation. The paper is organized as follow. Section II is devoted to the experimental methods used to measure CID cross-sections. The cross-section modeling is exposed in section III. Experimental CID results for the cluster sizes n=2 to n=6 are presented in section IV and analyzed with our model. The results are discussed in section V and the conclusions are given in section VI.

II. EXPERIMENTAL METHODS

A. Principle of TCID

In usual TCID setups, experiments are performed in ion guides and allow to perform collisions with large mass atoms such as Xenon without losing ions by deflection due to the collision. In order to determine unambiguously dissociation energies one has to take care of a number of experimental parameters. First, the number of collisions should be as low as possible in order to insure single collision conditions. This can be achieved by performing experiments at various pressures and extrapolating results to zero pressure. Second, one has to take care of possible so-called kinetic shifts that can alter the dissociation energy measurement. Indeed, at threshold collision energy, the system under study might not dissociate during the time scale of the experiment. The apparent threshold has therefore to be corrected. This is usually done by extrapolating the experimental values using RRKM dissociation rates. Third, the initial thermal energy distribution has to be taken into account. Finally, TCID experimental results are usually fitted assuming a given form for the CID cross-section, which can be expressed as[41]:

$$\sigma(E) = (\sigma_0 n/E) \sum_i g_i \int_{E_0-E_i}^{E} [1 - e^{-k(\varepsilon+E_i)\tau}] \times (E-\varepsilon)^{n-1} d\varepsilon \quad (1)$$

where σ_0 is the collision cross-section, n is the energy dependence of the reaction cross-section and E is the collision energy. The populations g_i of rovibrationnal states with energies E_i are used to carry out the thermal averaging. The dissociation rate k is usually calculated using RRKM type theories and τ is the typical experimental time between collision and detection. For comparison with experimental curves, Eq. 1 is further convolved with the kinetic energy distributions of both the ion and neutral reactants. If one needs to incorporate sequential fragmentation and/or competitive channels, these can also be included[42,43].

The method that is used in the following for the determination of the dissociation thresholds shows some differences with the well established method exposed above. First, we do not use ion guides. Therefore, we need to simulate the full ions trajectories in order to ensure that ion losses are correctly taken into account. Collisions are thus described with a microscopic model rather than with the average curve given by Eq. 1. This approach allows to include quite naturally sequential dissociation and potentially to test energy transfer models. Finally, one advantage of the used setup resides in the fact that the systems under

study are thermalized at low temperature prior to collisions. This implies that averaging over thermal energies of the parent ion plays a minor role, thus leads to minor uncertainties. For instance, for the largest size under study, n=6, the average internal energy is 13 meV at 25K.

B. Experimental setup

Collisions between mass selected pyrene clusters and different rare gases are performed using the experimental setup sketched in Figure 1. The operation principle of the setup has already been presented elsewhere.[44,45] Briefly, clusters are produced in a gas aggregation source[45] (a) and then thermalized (b) at 25 K through thousands of collisions with helium.

The experimental setup can be used in two modes. In the first mode, we make use of only the first Wiley-McLaren acceleration stage (c) together with the reflectron (i). Clusters are detected using dual micro-channel plates (MCP) (j) biased at -10 kV. This allows us to perform regular Time of Flight Mass Spectrometry (TOFMS) and to optimize the cluster production. In this mode, the mass filter (d), the electrodes for energy focusing (e) and deceleration (f), as well as the second Wiley-McLaren acceleration stage (h), are grounded.

FIG. 1. Schematic view of the experimental setup. (a) Cluster gas aggregation source. (b) Thermalization chamber. (c) First Wiley-McLaren acceleration stage. (d) Mass filter. (e) Energy focusing. (f) Deceleration. (g) Collision cell. (h) Second Wiley-McLaren acceleration stage. (i) Reflectron. (j) Micro-channel plate detector.

In the second mode, we make use of all the electrodes to mass select the clusters. In order to perform collisions between the mass selected clusters and the rare gas atoms, we make use of precisely delayed high voltages pulses applied to electrodes (c), (d), (e) and (f). Pulsed high voltages applied to the first Wiley-McLaren electrodes (c) accelerate all the clusters, giving them an average kinetic energy of 622 eV. The applied voltages and the spacing between the electrodes of the Wiley-McLaren are chosen such that, 26 cm

downstream, there is a linear relation (to first order) between the clusters position and their kinetic energy. Using a pulsed high voltage, an electric field is created in this region (e) that compensates this linear kinetic energy dispersion and all clusters have the same kinetic energy within a few eV. The time at which this pulsed high voltage is applied determines which cluster size is correctly energy focused. After this kinetic energy focusing, ions are decelerated by a potential barrier (f). At the end of the potential barrier, the potential is shut down in a field free zone and the mass selected clusters then fly freely through the collision cell (g) up to the second Wiley-McLaren acceleration stage (h). Clusters are then mass-analyzed using the reflectron (i) and the MCP detector (j). High voltage is applied on the mass filter (d) when the mass of interest enters the cylinder and shut down before it comes out. This allows to eliminate part of the neighboring masses. In the present experiments, the kinetic energy of the clusters in the laboratory frame is varied between 5 and 200 eV.

Kinetic energies of the ions can be easily deduced from experimental parameters. Indeed, since the distances in the apparatus are well known, by measuring for instance the time the ions take to travel from the end of the slowing down to the second acceleration stage gives us the speed of the ions. More precise kinetic energy calibration is obtained by recording the ions signal as a function of delays and/or voltages. These curves are then reproduced by simulations to obtain the kinetic energy distribution of the ions.[44]

C. Clusters production

Clusters are produced in a gas aggregation source previously described[45] ((a) in Figure 1). Pyrene powder (98% purity, Aldrich) is contained in an oven whose temperature is controlled. Typical oven temperature is 40 °C. The source is cooled down by a liquid nitrogen circulation. A controlled flow of helium gas is introduced in the source through the oven. The typical source pressure is about 1 mbar. Ionization takes place in the source by electron ionization. Electrons are emitted by a tungsten filament heated by a current of about 2.4 A. The filament is held at -150 V. Upon electron impact, ionization and dissociative ionization can occur. We indeed observe a fraction of mildly dehydrogenated cations (-H, -2H). In addition, minor fragments involving carbon loss ($C_{n=1-4}H_3$) are present, which indicates a contribution from rather energetic events[8,46–48].

FIG. 2. (a) Time of Flight Mass Spectrum of the clusters produced in the gas aggregation source. The main peaks are labeled. (b) TOF mass spectrum around the Py_2^+ peak. The thick black line is the experimental data. The columns bars represent the calculated intensities for the different peaks by taking into account the isotopic abundances.

Figure 2(a) gives an example of a TOF mass spectrum. The main peak appears to be due to the pyrene cation ($C_{16}H_{10}^+$, Py^+ in the following) and one can see mass peaks up to the tetramer cation (Py_4^+). Figure 2(b) presents the portion of the TOF-MS around the Py_2^+ peak at m/z=404.16. The peaks at m/z=405.16 and 406.17 correspond mainly to ^{13}C isotopologues of Py_2^+. The peaks at m/z=403.16, 402.15 and 401.15 correspond to the loss of 1, 2 or 3 hydrogen atoms.

The isotopes relative intensities can be calculated using:

$$I_{mass}^k = \frac{I_{mass}^0}{a^{n_C}} \frac{n_C!}{k!(n_C-k)!} a^{(n_C-k)}(1-a)^k \tag{2}$$

where $n_C = 32$ is the number of carbon atoms, k the number of ^{13}C atoms and $a = 0.9893$ the natural abundance of ^{12}C.

Because of the presence of dehydrogenated species and their isotopologues, each mass peak in Figure 2(b) can be written as the sum of several contributions:

$$I_{401} = I_{401}^0 \tag{3}$$

$$I_{402} = I_{401}^1 + I_{402}^0 \tag{4}$$

$$I_{403} = I_{401}^2 + I_{402}^1 + I_{403}^0 \tag{5}$$

$$I_{404} = I_{401}^3 + I_{402}^2 + I_{403}^1 + I_{404}^0 \tag{6}$$

$$I_{405} = I_{401}^4 + I_{402}^3 + I_{403}^2 + I_{404}^1 \tag{7}$$

$$I_{406} = I_{401}^5 + I_{402}^4 + I_{403}^3 + I_{404}^2 \tag{8}$$

From the measured intensities of I_{401} to I_{404}, we can deduce I_{401}^0 to I_{404}^0 and therefore predict the intensities of I_{405} and I_{406}. We can also deduce the contributions of the isotopo-

logues to the different peaks. The results are summarized in Figure 2(b) as column bars. The intensities of the two highest masses are well reproduced. We can see that for the peak corresponding to m/z=404, about 14% of the intensity comes from dehydrogenated species (12% -1H and 2% -2H).

The same procedure has been applied for sizes n=1 up to n=6 and total abundances could be derived for the dehydrogenated species as reported in Figure 3. The abundances are found to be relatively stable with cluster size, pure pyrene clusters accounting for about 60% of the population. The amount of triply dehydrogenated species is negligible whereas the abundance of doubly dehydrogenated species is quite stable with about 27% of the total intensity. More dispersion is observed for the singly dehydrogenated species with abundances ranging from 10% for n=4-5 up to 20% for n=1-2. These values are in line with the production in the source of dehydrogenated pyrene cations by dissociative ionization and their contribution to the nucleation of clusters.

In the following, the singly ($C_{16}H_9$) and doubly ($C_{16}H_8$) dehydrogenated pyrene molecules will be noted as Py-1H and Py-2H, respectively.

FIG. 3. Percentage of dehydrogenated and non-dehydrogenated species measured in the TOF-MS for $(Py)_n^+$ clusters, n=1-6.

D. Collisions

Once mass-selected and slowed down, the clusters fly freely through the collision cell. This cell is 5 cm long with an inner diameter of 2.5 cm. Clusters ions enter the cell through a 5 mm diameter hole while the exit hole has a 6 mm diameter. Two tubes of 1 cm diameter are attached to the side of the cell. One is used to introduce the gas whereas the other one is connected to two pressure gauges. We measure the pressure in the cell simultaneously with an ionization gauge and a capacitive gauge. Whereas the capacitive gauge is useful to get absolute values of the pressure for the different gases, the ionization gauge is used to record the pressure since it is more stable in our experimental conditions. We have used three

different collision gases, namely Helium, Neon and Argon, for which the pressures given by the ionization gauge have to be multiplied by a factor of 0.8, 4 and 6.7, respectively. The pressure has been kept as low as possible so that the number of collisions remains low. Typically, experiments have been performed with pressures below 10^{-4} mbar, keeping the estimated average number of collisions below 0.1.

The laboratory frame kinetic energy of the clusters can be varied from 5 to 200 eV. The kinetic energy distributions have an estimated full width at half maximum of about 4 eV.

The center of mass collision energy is given by:

$$E_{cm} = \frac{m}{M+m}E_k + \frac{3}{2}\frac{M}{M+m}k_B T_{cel} \tag{9}$$

where T_{cel} is the collision cell temperature at about 295 K. M is the cluster mass, m is the collision gas atom mass and E_k is the laboratory frame kinetic energy. The distribution of collision energies is the result of the convolution of the distribution of relative collision energies between the mass selected clusters and the gas atoms with the distribution of clusters kinetic energies. At high kinetic energy or low collision masses, the width of the distribution of collision energies is dominated by the Boltzmann thermal velocity distribution width. However, at 5 eV kinetic energy and for collisions with Argon, it is the kinetic energy distribution which dominates, with a width of 0.8 eV for 0.87 eV collision energy. However, the width is rapidly dominated by the thermal width as the collision energy is increased.

Figure 4 presents examples of TOF-MS obtained for the mass selection of Py_2^+ at a kinetic energy of 195 eV in the laboratory frame. At such a high kinetic energy, one can see that we were not able to mass select a single mass. Indeed, instead of having a single peak in Figure 4(b), we observe 5 peaks, which includes dehydrogenated species and their isotopologues. As will be discussed later in section IV B, the figure shows that the mass distribution is very similar to the one observed without mass selection in Figure 2(a). On the contrary, at 5 eV kinetic energy in the laboratory frame, we were able to mass select only one mass. Therefore, as the kinetic energy is varied, the number of peaks and their relative intensities change. In order to extract intensities and deduce cross sections in a reliable way, we have thus to model the evolution of peak intensities as the collision energy is varied. This modeling is described in the next section.

From the recorded peak intensities, absolute total fragmentation cross-sections can be derived as:

FIG. 4. Normalized TOF mass spectra resulting from the collision of pyrene dimer cations with Argon, Neon and Helium atoms for a kinetic energy of 195 eV in the laboratory frame. (a) Full TOF-MS for collisions with Argon. (b) Part of the TOF-MS around the parent peak. (c) Part of the TOF-MS around the Py^+ fragment peaks for collisions with Argon (black line), Neon (red line) and Helium (green line).

$$\sigma_{TOT} = -\frac{\mathbf{ln}(I/I_0)}{\rho l_{cell}} \tag{10}$$

where l_{cell} is the collision cell length and ρ is the atomic gas density. The intensities I and I_0 correspond to the parent intensity and the total parent plus fragment intensities, respectively. These intensities are extracted from the experimental TOF-MS by taking the peaks area. We use only the most intense peak to deduce the fragmentation cross-sections. The contribution of Py-1H and Py-2H ^{13}C isotopologues will be discussed in section IV B.

For sizes larger than n=2, several sequential fragmentation channels can be involved, such as:

$$\text{Channel 1: } Py_n^+ \rightarrow Py_{n-1}^+ + Py \tag{11}$$

$$\text{Channel 2: } Py_n^+ \rightarrow Py_{n-1}^+ + Py \rightarrow Py_{n-2}^+ + Py + Py \tag{12}$$

$$\text{Channel 3: } Py_n^+ \rightarrow Py_{n-1}^+ + Py \rightarrow Py_{n-2}^+ + Py + Py \rightarrow Py_{n-3}^+ + Py + Py + Py \tag{13}$$

$$... \tag{14}$$

$$\text{Channel n-1: } Py_n^+ \rightarrow Py_{n-1}^+ + Py \rightarrow ... \rightarrow Py^+ + (n-1)Py \tag{15}$$

Partial cross-sections for these fragmentation channels are obtained as:

$$\sigma_i = BR_i \sigma_{TOT} \tag{16}$$

where the branching ratios BR_i are given by

$$BR_i = \frac{I_i}{\sum_i I_i} \tag{17}$$

with I_i the intensity of the ith fragment peak.

We detail in the next section how the TOF-MS are simulated. The simulated TOF-MS are analyzed with the same tools as the experimental ones so that a direct comparison of the fragmentation cross-section can be achieved.

III. CROSS-SECTION MODELING

A. Trajectories calculation

TOF mass spectra are simulated by calculating trajectories of ions in the presence of the electric fields, which are calculated by solving numerically the Laplace equation. Equations of motion are integrated using the 4^{th} order Runge-Kutta method with adaptive step size.

An initial population of 50 000 ions is used. The masses of the ions are distributed so that the experimental mass distributions are reproduced, taking into account both the isotopic and dehydrogenated species abundances.

The ions initial positions are uniformly distributed in between the first two acceleration electrodes. A gaussian distribution is used for the initial velocities, with a central velocity of 600 m.s^{-1} and a width of 50 m.s^{-1}. The initial velocities distribution has been adjusted so that it reproduces the experimental kinetic energy distribution width and the time for applying the energy focalization voltage.

The initial internal energy of the clusters is distributed so that the ensemble of clusters have a canonical distribution of energy corresponding to a temperature of 25 K. At such a low temperature, there is no thermal evaporation before the clusters undergo a collision.

At each time step the collision and dissociation probability are evaluated. For the collisions, we calculate the collision rate as:

$$\Gamma_{coll} = \rho \sigma_{geo} v_{rel} \tag{18}$$

with ρ the gas density in the collision cell, σ_{geo} the geometric cross-section and v_{rel} the relative velocity between the atoms of the gas and the cluster. The atom velocities are distributed according to the Boltzmann distribution.

Upon collision, part of the collision energy is transferred to the cluster internal energy. We use the Line of Center (LOC) model[49] to calculate the energy transfer (see below). After

the collision, the cluster velocities are calculated so that the conservation of momentum is constrained.

B. Energy transfer

In order to evaluate the amount of collision energy transferred into internal energy, we make use of the LOC model[49]. In this model, one assumes that the transferred energy E_t is the collision energy E_c diminished by the centrifugal energy:

$$E_t = \frac{1}{2}\mu v_{radial}^2 = E_c(1 - \frac{b^2}{R^2}) \tag{19}$$

where μ is the reduced mass of the cluster + atom system, b is the impact parameter and R is the cluster radius. v_{radial} is the radial component of the relative velocity between the cluster and the atom. When the statistical distribution of impact parameters is taken into account, the distribution of deposited energy is uniform between 0 and the maximum available energy, that is, the collision energy E_c.

We are aware that this model is quite crude. However, evaluating the energy transfer in a realistic way is beyond the scope of this paper. Several studies have shown that the use of the so-called modified LOC model can be successfully used to fit TCID cross-sections[50–52]. This modified LOC model introduces an extra adjustable parameter (n in Eq. 1) to take into account the kinetic energy dependence of the collision energy transfer. As will be shown, the simple LOC model with $n = 1$ allows reproducing satisfactorily our experimental results.

After a collision, the internal energy of the clusters is increased and their dissociation rate is evaluated as described in the next section.

C. Dissociation rate

The clusters dissociation rate is evaluated using PST. We have already used this model in a previous paper[38] to model the thermal evaporation of pyrene cluster cations. Briefly, the J-conserved dissociation rate is evaluated as[53]:

$$W(E, J) = \frac{(\alpha_f/\alpha_b)G(E_f, J)}{h(2J+1)N(E)} \tag{20}$$

$$E_f = E + E_{rot} - D \tag{21}$$

$$E_{rot} = B_0 J(J+1) \tag{22}$$

where E is the initial internal vibrational energy of the parent cluster, E_{rot} is its initial rotational energy, J is its initial total angular momentum, and B_0 is its rotational constant. E_f is the total (internal+ external) energy of the fragments. D is the dissociation energy. α_f and α_b are the forward and backward reaction path degeneracies, respectively. Their ratio is taken equal to 1. The density of states $N(E)$ and the total number of states $G(E_f)$ are obtained by inversion of the partition function using the steepest descent method under the constraint of total angular momentum conservation and the hypothesis of loose transition state. The version of the PST used here takes into account conservation of both energy and total angular momentum. It assumes that the transition state is defined at the maximum of the centrifugal barrier (loose transition state). Only harmonic vibrations are considered, and parent and products are considered to have spherical symmetry. The use of the PST allows not only to calculate the dissociation rate but also to get the energy partitioning between internal energies of the fragments, their relative kinetic energy and their rotational energies. This allows in particular to investigate the fragmentation of large clusters and to reproduce the cascade of dissociation occurring after collision.

Having access to the relative kinetic energy upon dissociation allows in particular to include the influence of dissociation on the ion trajectories.

All the needed ingredients for the PST calculation (harmonic frequencies and moments of inertia) are taken from DFTB-CI calculations[39] as in our previous work on thermal evaporation[38]. For sake of clarity, note that the theoretical dissociation energies discussed hereafter always correspond to the differences between the energies of global minima of parents and fragments, disregarding dissociation from or toward secondary minima.

The dissociation of clusters containing dehydrogenated species is considered to occur with the same rate and the same dissociation energy as the normal pyrene clusters. As will be shown in section IV B, simple rules regarding the dissociation of dehydrogenated species can be drawn. For the dimer, in the case of doubly dehydrogenated species, both fragments have an equal probability to carry the charge. Namely Py-Py-2H can either dissociate into Py^++Py-2H or Py + Py-$2H^+$. For singly dehydrogenated species, the charged fragment is Py^+. We have generalized these rules for larger sizes: doubly dehydrogenated species have the same probability as normal species to be ejected upon dissociation, whereas the singly dehydrogenated species are always first ejected.

As will be shown later in section IV, the partition among the different fragmentation

channels for n>3 needs an additional relaxation path to be included. Namely, we have to assume that after the first initial dissociation some of the clusters do not dissociate anymore. In the calculation, the non-dissociating clusters are randomly chosen with a given weight and their energy is set to zero after the first initial dissociation. Possible origins for this additional relaxation process are provided in section V.

D. Comparison of trajectories calculations with experimental results

The end results of our trajectories calculations consist in TOF-MS for each collision energy. These data are analyzed with the same tools as the ones used to analyze the experimental results. We have checked that we satisfactorily reproduce the widths and the positions of the peaks in the TOF-MS. In particular, as the kinetic energy of the clusters is varied, their TOF after the second Wiley-Mc Laren acceleration varies due to the change in initial velocity. The time position of the parent peaks is well reproduced by our calculations, demonstrating the ability of the trajectory calculations to reproduce the experimental kinetic energies.

Peak intensities are extracted from the TOF-MS by taking the peaks area. We keep only the most intense peak in both the parent and the fragments to calculate the cross-sections. This way we minimize the influence of the dehydrogenated species in our cross-section determination.

Our final results consist in total and partial fragmentation cross-section measured as a function of the collision energy. For the total fragmentation cross-section, there are only two parameters that need to be adjusted to reproduce the experimental total cross-section, namely the geometrical cross-section and the dissociation energy. For sizes n>2, several fragmentation channels are involved as discussed in Section II D. In order to reproduce the partial cross-sections corresponding to these, the corresponding dissociation energies have also to be adjusted. Finally, in order to have the correct relative intensities between the partial cross-sections an additional parameter is introduced to include the additional relaxation channel introduced in the previous section.

In order to reproduce the experimental results, these parameters have been adjusted by trial and error. We needed to run few calculations only in order to get a satisfactory agreement with experiment.

IV. COLLISION INDUCED DISSOCIATION RESULTS

A. Dimer

FIG. 5. Fragmentation cross-section of the pyrene dimer cation as a function of the center of mass collision energy. The collision gas is (a) Argon, (b) Neon and (c) Helium. The red squares are the experimental data whereas the blue line is the result of the model discussed in the text. In (a) the black line is the theoretical cross-section convolved with the distribution of collision energies.

Figures 5(a), (b) and (c) present the measured absolute fragmentation cross-section as a function of the center of mass collision energy E_{cm}, for collisions with Argon, Neon and Helium, respectively. In these figures, both the experimental data and the results of the modeling are displayed. Similar trends are observed in all figures: (i) At low collision energy, no fragmentation is observed. (ii) As the collision energy is increased, fragmentation appears and the measured cross-section increases rather steeply. (iii) As the collision energy is further increased, the cross-section flattens somewhat. We therefore observe in these curves a threshold for fragmentation that can be related to the dissociation energy of the cluster. To check this, we have used the model presented in section III to try to reproduce our experimental data. We have fixed the dissociation energy value at 1.07 eV, as predicted by Dontot *et al.* for Py_2^+[39]. A good agreement is obtained between experiment and modeling. In order to reproduce the experimental results, the geometrical cross-sections have been taken equal to 63, 59 and 45 Å^2 for collisions with respectively Argon, Neon and Helium. Assuming that the geometrical cross-section can be written as:

$$\sigma_{geo} = \pi(R + r_X)^2 \tag{23}$$

with R the cluster radius and r_X the collision atom radius, with X =Ar, Ne or He. Taking r_X as the van der Waals radii for the atoms, one can deduce the radius R as $R = \sqrt{\sigma/\pi} - r_X$. With $r_{Ar} = 1.88$ Å, $r_{Ne} = 1.54$ Å and $r_{He} = 1.4$ Å, this leads to respective values for R of 2.8, 2.6 and 2.4 Å. For Ar and Ne, the difference in the cross sections can be almost fully accounted for by the difference in the collider radius. For He, the agreement is not completely

satisfactory. However, given the uncertainties in the pressure measurements, especially with Helium, one can consider that the agreement between the three values remains satisfactory.

The relative low value of the apparent cross-section with Argon in Figure 5(a) at high energy is due to the loss of some of the fragments: the Argon mass is large enough to induce significant deflection of the ions upon collisions. If the deflection is important, the ions do not eventually reach the detector. This is why we measure an apparently weaker cross-section for Argon. However, since these deflections are taken into account in the trajectories simulations, we can still deduce from them the "real" cross section. To illustrate this, we have plotted in Figure 5(a) the theoretical cross-section convolved with the relative kinetic energies distribution. One can clearly see the effect of the kinetic shift and that at high collision energies the theoretical cross-section is higher than the measured one.

We emphasize that apart from the value of the geometrical cross-section there is no free parameter in our model. In particular, the dissociation energy is directly taken from the theoretical study of Dontot *et al*[39]. A very good agreement is therefore obtained between the predicted dissociation energy and our observation.

B. Dehydrogenated dimers

FIG. 6. Experimental intensities extracted from Figure 4(c) together with intensities calculated using the three hypotheses described in the text.

Figure 4 presents the TOF-MS of the mass selected dimer pyrene cation at a kinetic energy of 195 eV in the laboratory frame. At such a high kinetic energy, as already mentioned, our device does not allow to mass select a single mass. Indeed, one can see several peaks corresponding to the presence of dehydrogenated species and isotopologues. The intensities of the different peaks are very similar to the ones presented in Figure 2(b). This means that in the present case our mass selection allows us to study the fragmentation of all the species at once without altering the relative peak intensities.

Figure 4(c) presents the recorded fragment peaks around the mass of Py^+. The fragmentation experiment has been performed for three different collision gases, namely Argon, Neon and Helium. This leads to center of mass collision energies of 17.5, 9.2 and 1.9 eV. Very similar fragmentation patterns are obtained for the three gases despite the rather different collision energies. One can see that the relative intensities are quite different from the ones of the parent. In particular, there is a rather clear loss of intensities for the singly dehydrogenated species. One can try to reproduce the intensities of the fragment peaks using the ones of the parent under the following hypothesis. First, we assume that the doubly dehydrogenated clusters dissociate into Py^++Py-2H or Py+Py-$2H^+$ with the same probability. For the singly dehydrogenated pyrene dimer, we have made the three following hypotheses:

1. Hypothesis 1: $(Py\text{-}Py\text{-}1H)^+ \rightarrow Py^+ + Py\text{-}1H$.
2. Hypothesis 2: $(Py\text{-}Py\text{-}1H)^+ \rightarrow Py^+ + Py\text{-}1H$ and $(Py\text{-}Py\text{-}1H)^+ \rightarrow Py + Py\text{-}1H^+$ with the same probability.
3. Hypothesis 3: $(Py\text{-}Py\text{-}1H)^+ \rightarrow Py + Py\text{-}1H^+$

Intensity partition among the different isotopologues is taken into account according to the above hypotheses. The resulting fragment intensities are reported in Figure 6 together with the experimental intensities resulting from the integration of the peaks in Figure 4(c).

From inspection of Figure 6, it appears that hypotheses (2) and (3) predict far too large intensity for fragments at m/z=201. Hypothesis (1) provides therefore the most likely channel. This is further supported by DFT calculations which predict that Py-1H has a higher ionization energy than Py by about 0.4 eV[54]. We have performed additional calculations of the adiabatic ionization energy at the MP2 and CCSD levels that confirm this difference in ionization energy. Our observed dissociation path is therefore consistent with the charge remaining on the fragment with the lowest ionization energy. We note however that we cannot completely reproduce the intensity of the m/z=201 peak, which suggests that a fraction of species follow the channels given by Hypotheses (2) and (3).

It has been predicted that covalent bonds are promptly formed within pyrene dimers upon dehydrogenation[7,8]. In our experiments, the experimental abundances can be fairly well reproduced by assuming that clusters containing dehydrogenated pyrene units dissociate

the same way as clusters made of pure pyrene units, we have therefore no evidence for the formation of covalent bonds. The absence of covalent bonds is likely due to the fact that our formation conditions are less energetic than the ones in the experiment by Zhen *et al.*[8]. In order to further investigate this point, we have performed CID measurements by mass selecting the Py-Py-1H and Py-Py-2H cations. The corresponding CID curves are given in Figure 7. The threshold for dissociation appears to be very similar for the three curves. The observed difference in the cross-section asymptotic value between the normal and dehydrogenated clusters comes from the imperfect mass selection: as the kinetic energy is increased, more and more larger sizes come into play and therefore more fragments appear that are due to the fragmentation of these larger masses. This is less important when considering the normal pyrene dimer as it is the most abundant species. However, when it comes to the dehydrogenated species, this is not true anymore.

FIG. 7. Fragmentation cross-section of the pyrene dimer cation and its dehydrogenated forms -1H and -2H as a function of the center of mass collision energy. Collision gas is Argon. Blue squares are the experimental data for Py_2^+, the green line is for Py-Py-2H$^+$ and the red line for Py-Py-1H$^+$.

C. Trimer

Experimental fragmentation cross sections as a function of collision energy for Py_3^+ colliding with Argon are presented in Figure 8. There are two channels:

$$\text{Channel 1: } Py_3^+ \rightarrow Py_2^+ + Py \tag{24}$$

$$\text{Channel 2: } Py_3^+ \rightarrow Py_2^+ + Py \rightarrow Py^+ + Py + Py \tag{25}$$

The results of the trajectories simulations are plotted together with the experimental data in Figure 8(a). A good agreement is obtained with the experiment by taking the theoretical values of the dissociation energies[39], namely 1.077 eV and 0.791 eV for Py_2^+ and Py_3^+, respectively. In order to reproduce the total cross-section, the geometrical cross-section is taken equal to 95 Å^2. We note that although the total cross-section and the thresholds

are well reproduced, our model fails to perfectly reproduce the relative intensity for the two fragmentation channels.

In order to obtain the good agreement between the model and the experiment as presented in Figure 8(b), one has to assume that about 30% of Py_2^+ do not dissociate. Apart from this additional relaxation path, the other parameters are kept the same. In the following, we will only show the simulation results with this additional relaxation path included. In the following, for the larger species, we will only show the simulation results with this additional relaxation path included, which does not affect the threshold energies neither the total cross sections.

We note that the apparent threshold for the first dissociation lies just below the calculated bond energy, a consequence of the energy distributions. In contrast, the second threshold lies well above the calculated energy (1.87 eV), a result of the kinetic shift, which of course is seen in many such experiments[41].

FIG. 8. Experimental fragmentation cross-section (squares) together with the theoretical one (lines) for Py_3^+ colliding with Argon. Channel $Py_3^+ \rightarrow Py_2^+$+Py is represented in black and channel $Py_3^+ \rightarrow Py^+$+Py+Py in red. The total cross-section is plotted in blue. Simulations are given (a) without and (b) with an additional relaxation path (see text for details).

D. Tetramer

Cross-section measurements for Py_4^+ are displayed in Figure 9. We have now three channels for dissociation, namely:

$$\text{Channel 1: } Py_4^+ \rightarrow Py_3^+ + Py \tag{26}$$

$$\text{Channel 2: } Py_4^+ \rightarrow Py_3^+ + Py \rightarrow Py_2^+ + Py + Py \tag{27}$$

$$\text{Channel 3: } Py_4^+ \rightarrow Py_3^+ + Py \rightarrow Py_2^+ + Py + Py \rightarrow Py_1^+ + Py + Py + Py \tag{28}$$

In order to reproduce the experimental results, the geometrical total cross-section in the simulations is taken equal to 113 $Å^2$. Here, the calculated dissociation energy of a

FIG. 9. Experimental fragmentation cross-section (squares) together with the theoretical ones (lines) for Py_4^+ colliding with Argon. Channel $Py_4^+ \rightarrow Py_3^+ + Py$ is represented in black, channel $Py_4^+ \rightarrow Py_2^+ + Py + Py$ in red and channel $Py_4^+ \rightarrow Py^+ + Py + Py + Py$ in green. The total cross-section is plotted in blue.

neutral pyrene molecule from Py_4^+ calculated by Dontot *et al.*[39] does not allow to reproduce the experimental results. Instead, we have found that our experimental results are best reproduced by using a dissociation energy of 0.68 eV for Py_4^+. For the other dissociation channels, we have taken the already determined values of 0.791 and 1.077 eV for Py_3^+ and Py_2^+ respectively.

Using this value for the dissociation energy of Py_4^+, the total cross-section is well reproduced by our trajectories simulations as can be seen in Figure 9. Concerning partial cross-sections, the agreement between simulations and experimental results remains satisfactory but not as good.

In order to have a correct amplitude for the channel 1 cross-section, we had to include a contribution from the relaxation path that breaks the dissociation cascade. Its contribution was estimated to be 15% of the dissociation events. Concerning channels 2 and 3, the threshold for the appearance of fragments Py_2^+ and Py^+ are correctly reproduced but the amplitudes are not well reproduced at high collision energy.

E. Pentamer

Figure 10 presents the experimental results together with the simulation results for the CID cross-section of Py_5^+ as a function of the collision energy. Each threshold corresponding to the successive losses of neutral pyrene molecules is clearly observable. In order to reproduce the experimental results we have used a geometrical cross-section of 162 Å and a dissociation energy of 0.75 eV for Py_5^+, which is 0.11 eV lower than the theoretical prediction. For the smaller clusters involved in the dissociation cascades, we have kept the previously validated dissociation energies. As for the tetramer, a better agreement is obtained by

FIG. 10. Experimental fragmentation cross-section (squares) together with the theoretical ones (lines) for Py_5^+ colliding with Argon. Channel $Py_5^+ \rightarrow Py_4^+$+Py is represented in black, channel $Py_5^+ \rightarrow Py_3^+$+Py+Py in red, channel $Py_5^+ \rightarrow Py_2^+$+Py+Py+Py in green and channel $Py_5^+ \rightarrow Py^+$+Py+Py+Py+Py in blue. The total cross-section is plotted in magenta.

assuming that 15% of the initial dissociation events do not lead to further dissociation.

Similarly to the tetramer, there are some discrepancies between the present simulation and experiment at high collision energies in the relative amplitudes of the partial cross-sections. However, once again the appearance thresholds for the different channels are fairly well reproduced.

F. Hexamer

FIG. 11. Experimental fragmentation cross-section (squares) together with the theoretical ones (lines) for Py_6^+ colliding with Argon. Channel $Py_6^+ \rightarrow Py_5^+$+Py is represented in black, channel $Py_6^+ \rightarrow Py_4^+$+Py+Py in red, channel $Py_6^+ \rightarrow Py_3^+$+Py+Py+Py in green, channel $Py_6^+ \rightarrow Py_2^+$+Py+Py+Py+Py in blue and channel $Py_6^+ \rightarrow Py^+$+Py+Py+Py+Py+Py in magenta. The total cross-section is plotted in dark yellow.

Figure 11 presents the experimental results together with the simulation results for the CID cross-section of Py_6^+ as a function of the collision energy. In order to reproduce the experimental results we have used a geometrical cross-section of 176 Å^2 and a dissociation energy of 0.72 eV for these cations, which is 0.16 eV lower than the theoretical prediction.

Again, a better agreement is obtained for the partial cross-sections by assuming that 15% of the initial dissociation events do not lead to further dissociation.

The second dissociation threshold from Py_6^+ is lower than the one observed for Py_5^+. In order to reproduce the threshold appearance of the Py_4^+ cation, we had to use in the simulations a dissociation energy of 0.65 eV for $Py_5^+ \rightarrow Py_4^+ + Py$. However, for the other smaller clusters, we managed to keep the previously deduced dissociation energies. Similarly to the previous cases, the agreement between experiments and simulations degrades as the collision energy is increased.

V. DISCUSSION

We have plotted in Figure 12 the geometrical cross-sections used in the simulations to reproduce the measured cross-sections. In order to have an estimation of the geometrical cross-section we have determined the solvent accessible surface and the molecular surface from the DFTB-CI structures. We have used a solvent radius of 1.88 Å corresponding to the Argon atom. The obtained surfaces using Jmol[55] are almost convex and we therefore use the Cauchy's Surface Area Formula[56] to deduce the averaged projected surface area as being 1/4th of the total surface area. The results of the application of the Cauchy's formula are given as lines in Figure 12. The geometrical cross-section deduced from the solvent accessible surface is about twice the experimental value whereas that deduced from the molecular surface gives a good agreement with experiment. This could mean that the impact parameter has to be within the molecular surface for efficient enough energy transfer to occur. In other words, grazing collisions, even at high collision energy, do not lead to fragmentation. Alternatively, one could also consider that the experimental determination of the cross-section is off by a factor of 2. In the case of the dimer, as already mentioned in section IV A, we find variations in the cross-section as a function of the collision gas that can be accounted for by the collision atom radii. This tends to imply that the apparent radius of the pyrene clusters for CID is much smaller than the one predicted by the molecular or solvent accessible surface. This discrepancy might come from the fact that these surfaces are built based on van der Waals radii, whereas collision energy transfer might occur on a much shorter length scale. Finally, in an ion mobility study Beitz *et al*[57] have measured diffusion cross-sections for various PAH dimer cations. By extrapolating their results to the pyrene dimer cation, one can deduce from their study a diffusion cross-section of about 130 Å^2.

Figure 13 summarizes our results regarding the determination of the dissociation energies

FIG. 12. Geometrical cross-sections used to reproduce the experimental fragmentation cross-section (squares) together with the average projected area deduced from the DFTB-CI structure calculation (lines). The red line is deduced from the molecular surface whereas the black line is from the solvent accessible surface.

FIG. 13. Experimentally determined dissociation energies in this work (red squares) together with the ones determined in ref. 38 (blue squares) as a function of cluster size. The lines are for the theoretical dissociation energies. The upper branch corresponds to dissociation energies calculated as the energy difference between lowest energy structure. The lower branch is calculated as the energy difference between stack structures.

of cationic pyrene clusters. The TCID experimental results are compared both with our previously determined dissociation energies through thermal evaporation rates measurement[38] and with the theoretically calculated dissociation energies. The agreement between the two experimental data sets is within 0.1 eV, which reinforces our confidence in the derived values considering that the two techniques are significantly different. The theoretical values of the dissociation energies have been calculated for the lowest energy structures of the charged clusters, but also for stack isomers. Stack structures were found as higher energy metastable isomers in the DFTB-CI search[39]. The results of both calculations lead to the two branches displayed in Figure 13. For the two smallest sizes the dissociation energies are the same since the stack structures are the most stable ones. In addition, there is an excellent agreement with experimental values. For size n=4 we find that the dissociation energy assuming stack structures remarkably matches the experimental value, despite the fact that from this size to larger ones, stack structures are not the most stable anymore. For the larger sizes, the experimental values fall in between both theoretical models with a typical difference of 0.2 eV. Despite this difference, we find a similar trend in both experiment and theory, with

a decrease of the dissociation energy from n=2 to n=3, before reaching a plateau for the larger sizes. The initial decrease is well understood in terms of charge resonance enhanced stability of the dimer with respect to the trimer. When increasing size, the contribution of charge resonance to the cluster stability still decreases on the opposite to the contribution of dispersion interactions. Both contributions strongly depend on steric effects, which may result in non-monotonous evolution of the dissociation energies with sizes.

The observed difference between experiment and theory can have various origins. First, the employed theoretical method is approximate and although the DFTB-CI results seem to agree with the experimental ones for the lowest sizes, one cannot exclude that the theory is somehow less accurate at larger sizes due to its inherent approximations. Furthermore, despite the effort to explore the potential energy surface in order to find the global minimum, there is always a possibility that this minimum is missed. This is obviously more probable for increasing cluster sizes. However, stack structures are certainly correct for n=2 and 3. For larger sizes, if the correct ground state is not found, this would only increase the discrepancy with experiment.

Second, even if the predicted lowest energy structures are correct, and consistently their theoretical energy differences, it is still possible that part of the clusters are produced in the ion source with structures which are not the lowest predicted structures. This scenario was already discussed in our previous study[38]. As discussed in section II C, we have evidence through the results on dehydrogenated species that nucleation is kinetically controlled by pyrene cations and their dehydrogenated counterparts. The growth is then expected to proceed by sequential addition of pyrene molecules. Since this growth occurs at low temperature, it is possible that not all possible structures are explored and that isomers at higher energies than the global minimum can be produced. This scenario is consistent with the experimental values of the dissociation energies falling between the two calculated branches. The stacked structures are indeed found at increasing energies above the lowest-energy structures as size increases[39]. The difference in dissociation energies between the two calculated structures can therefore be considered as indicative of the possible dispersion of these values depending on isomer structures.

Third, imperfect thermalization could be invoked as a possible source of higher initial internal energy. However, in order to reconcile experiment with theory, the initial temperature should be 160 K for size n = 5 for example. Such a high initial temperature is highly

unlikely given the 25 K temperature of the thermalization stage.

However, we note that, up to the pentamer, the thresholds for the sequential dissociation are well reproduced by using the very same input dissociation energies for sizes n=2 to n=5. It is only for the size n=6 that we had to assume a different dissociation energy, and only for the n=5 to n=4 fragmentation, the other thresholds being well reproduced. This means that from n=2 to 5, we observe a single dissociation sequence, implying in particular that when going from n=5 to n=4 or starting with n=4, the same structure is produced for n=4, or at least structures with the same dissociation energy. This could imply that for sizes n=2 to n=5, the dissociation cascade proceeds through the same structures as the ones being produced in the source. It is only for the size n=6 that dissociation would lead to a n=5 cluster with a somewhat different structure from the one of the parent ions produced in the source. This would be in favor of clusters produced in the lowest energy structures as one would expect that upon collision energy deposition dissociation would proceed through lowest energy structures. Nevertheless, one can not exclude the possible competition with isomerization in the course of dissociation.

We have mentioned several times that in order to reproduce the experimental relative intensities between the different fragmentation channels, we assumed that part of the initial fragments did not undergo fragmentation anymore:

$$\text{Channel 1: } \mathrm{Py}_n^+ \rightarrow \mathrm{Py}_{n-1}^{*+} + \mathrm{Py} \tag{29}$$

$$\text{Channel 1': } \mathrm{Py}_n^+ \rightarrow \mathrm{Py}_{n-1}^{+} + \mathrm{Py} \tag{30}$$

$$\text{Channel 2: } \mathrm{Py}_n^+ \rightarrow \mathrm{Py}_{n-1}^{*+} + \mathrm{Py} \rightarrow \mathrm{Py}_{n-2}^{**+} + \mathrm{Py} + \mathrm{Py} \tag{31}$$

$$... \tag{32}$$

$$\text{Channel n-1: } \mathrm{Py}_n^+ \rightarrow \mathrm{Py}_{n-1}^{*+} + \mathrm{Py} \rightarrow ... \rightarrow \mathrm{Py}^+ + n\mathrm{Py} \tag{33}$$

where Channel 1' corresponds to a dissociation with not enough energy left in the Py_{n-1}^+ fragment to dissociate. This hypothesis allowed us to obtain a good description of the first two dissociation channels. However, we noted that as the collision energy increased, the intensities between subsequent channels were less and less well described. Similarly to the hypothesis made for the initial dissociation, we suspect that additional channels opening occur that are not taken into account and that could explain the observed discrepancies.

One possible explanation for the first channel could be that part of the collisions lead to a rather direct dissociation, leaving the charged fragment with too little internal energy to

further evaporate. This hypothesis is able to explain the initial correction in the relative fragmentation channels intensities but not the deviations at high collision energies for the other channels.

The observed deviations at high collision energies could come in part from erroneous evaluation of the energy partitioning upon dissociation. The imperfect prediction of the energy partitioning getting worse as more and more dissociation take place.

Another explanation could be that isomerization processes occur during dissociation or compete with dissociation, leading to different fragmentation channels not taken into account. This could also be related to the ability of the excited clusters to overcome isomerization barriers. Such processes would alter the relative intensities between the different channels.

Finally, we note that, in reference 43, the authors had to similarly introduce a scaling factor for reducing the probabilities of sequential dissociation. The origin of this effect is still to be elucidated but it might be a common phenomenon rather than a particular feature of this experiment.

VI. CONCLUSION

In the present work, we have experimentally addressed the stability of cationic pyrene clusters in the range n=2-6 using the TCID technique, an independent alternative to the thermal evaporation technique used in our previous work. The derived values for the dissociation energies were found to be in excellent agreement between the two types of experiments, within an accuracy of 0.1 eV. Comparison with theoretical values shows an excellent agreement for n=2 and 3, while for larger sizes, DFTB-CI values fall above experimental ones by 0.2 eV. This difference might be related to the approximations inherent to the electronic structure calculation method. From the experimental side, this can also be the sign that the growth process does not necessarily form the lowest energy structures. Discrepancies in the relative intensities between the dissociation channels point towards the existence of additional dissociation channels that were not taken into account. Competition between isomerization and dissociation or the presence of direct dissociation have been evoked as a possible explanations.

In addition to homogeneous pyrene cation clusters, we have also addressed the fragmen-

tation of clusters containing dehydrogenated species. We concluded that the stability of these clusters is comparable to their homogeneous counterparts, pointing to the absence of covalent bounds, both at the formation and upon dissociation.

We have shown that the use of the TCID technique combined with modeling opens perspectives to study the dissociation of PAH cluster cations and derive their dissociation energies. An extension of the present work would certainly be to address larger sizes in order to check the thermal evaporation results in a larger range possibly bridging the gap between small clusters and bulk. The present experimental work also calls for further theoretical studies, such as structural investigations and stability of dehydrogenated species versus dissociation. In general, the determination of dissociation paths and barriers including isomerization barriers would be of interest. Finally, molecular dynamics simulations of the collisions would potentially allow to investigate both the initial collision energy transfer and the nature of the fragmentation. Such simulations, although computationally very costly for the large cluster sizes, could be started for the smaller systems, for instance a pyrene dimer colliding with Argon.

ACKNOWLEDGMENTS

This work received support from the European Research Council under the European Union's Seventh Framework Programme ERC-2013-SyG, Grant Agreement no. 610256, NANOCOSMOS.

DATA AVAILABILITY

The data that supports the findings of this study are available within the article.

REFERENCES

[1]A. Léger and J. L. Puget, "Identification of the 'unidentified' IR emission features of interstellar dust?" Astron. Astrophys. **137**, L5–L8 (1984).

[2]L. J. Allamandola, A. G. G. M. Tielens, and J. R. Barker, "Polycyclic aromatic hydrocarbons and the unidentified infrared emission bands - Auto exhaust along the Milky Way," Astrophys. J. Lett. **290**, L25–L28 (1985).

[3]M. Rapacioli, C. Joblin, and P. Boissel, "Spectroscopy of polycyclic aromatic hydrocarbons and very small grains in photodissociation regions," Astron. Astrophys. **429**, 193–204 (2005).

[4]O. Berné, C. Joblin, Y. Deville, J. D. Smith, M. Rapacioli, J. P. Bernard, J. Thomas, W. Reach, and A. Abergel, "Analysis of the emission of very small dust particles from Spitzer spectro-imagery data using blind signal separation methods," Astron. Astrophys. **469**, 575–586 (2007).

[5]P. Pilleri, J. Montillaud, O. Berné, and C. Joblin, "Evaporating very small grains as tracers of the UV radiation field in photo-dissociation regions," Astron. Astrophys. **542**, A69 (2012).

[6]R. Delaunay, M. Gatchell, P. Rousseau, A. Domaracka, S. Maclot, Y. Wang, M. H. Stockett, T. Chen, L. Adoui, M. Alcamí, F. Martín, H. Zettergren, H. Cederquist, and B. A. Huber, "Molecular growth inside of polycyclic aromatic hydrocarbon clusters induced by ion collisions," J. Phys. Chem. Lett. **6**, 1536–1542 (2015).

[7]T. Chen, "Formation of Covalently Bonded Polycyclic Aromatic Hydrocarbons in the Interstellar Medium," The Astrophysical Journal **866**, 113 (2018).

[8]J. Zhen, T. Chen, and A. G. G. M. Tielens, "Laboratory Photochemistry of Pyrene Clusters: An Efficient Way to Form Large PAHs," The Astrophysical Journal **863**, 128 (2018).

[9]M. Rapacioli, F. Calvo, C. Joblin, P. Parneix, D. Toublanc, and F. Spiegelman, "Formation and destruction of polycyclic aromatic hydrocarbon clusters in the interstellar medium," Astron. Astrophys. **460**, 519–531 (2006).

[10]J. Montillaud and C. Joblin, "Absolute evaporation rates of non-rotating neutral polycyclic aromatic hydrocarbon clusters," Astron. Astrophys. **567**, A45 (2014).

[11]M. Rapacioli and F. Spiegelman, "Modelling singly ionized coronene clusters," Eur. Phys. J. D **52**, 55–58 (2009).

[12]C. Joblin, L. Dontot, G. A. Garcia, F. Spiegelman, M. Rapacioli, L. Nahon, P. Parneix, T. Pino, and P. Bréchignac, "Size effect in the ionization energy of pah clusters," The Journal of Physical Chemistry Letters **8**, 3697–3702 (2017).

[13]M. Schmidt, A. Masson, and C. Bréchignac, "Coronene cluster experiments: Stability and thermodynamics," Int. J. Mass Spectrom. **252**, 173–179 (2006).

[14]H. A. B. Johansson, H. Zettergren, A. I. S. Holm, F. Seitz, H. T. Schmidt, P. Rousseau, A. Ławicki, M. Capron, A. Domaracka, E. Lattouf, S. Maclot, R. Maisonny, B. Manil,

J.-Y. Chesnel, L. Adoui, B. A. Huber, and H. Cederquist, "Ionization and fragmentation of polycyclic aromatic hydrocarbon clusters in collisions with kev ions," Phys. Rev. A **84**, 043201 (2011).

[15]S. O. Baek, R. a. Field, M. E. Goldstone, P. W. Kirk, J. N. Lester, and R. Perry, "A review of atmospheric polycyclic aromatic hydrocarbons: Sources, fate and behavior," Water Air Soil Pollut **60**, 279–300 (1991).

[16]C.-T. Li, H.-K. Zhuang, L.-T. Hsieh, W.-J. Lee, and M.-C. Tsao, "Pah emission from the incineration of three plastic wastes," Environ. Int. **27**, 61–67 (2001).

[17]M. Blanchard, M.-J. Teil, E. Guigon, K. Larcher-Tiphagne, D. Ollivon, B. Garban, and M. Chevreuil, "Persistent toxic substance inputs to the river seine basin (france) via atmospheric deposition and urban sludge application," Sci. Total Environ. **375**, 232–243 (2007), human activity and material fluxes in a regional river basin: the Seine River watershed Seine Special Issue.

[18]A. Birgül, Y. Tasdemir, and S. S. Cindoruk, "Atmospheric wet and dry deposition of polycyclic aromatic hydrocarbons (pahs) determined using a modified sampler," Atmos. Res. **101**, 341–353 (2011).

[19]A. D. P. Netto, T. M. Krauss, I. F. Cunha, and E. C. Rego, "Pahs in sd:polycyclic aromatic hydrocarbons levels in street dust in the central area of niterói city, rj, brazil," Water Air Soil Pollut **176**, 57–67 (2006).

[20]D. Phillips, "Fifty years of benzo(a)pyrene." Nature **303**, 468–472. (1983).

[21]T. M. Penning, M. E. Burczynski, C.-f. Hung, K. D. Mccoull, N. T. Palackal, and L. S. Tsuruda, "Hydrocarbon Activation : Generation of Reactive and Redox Active o -Quinones," Chem. Res. Toxicol. **12**, 1–18 (1999).

[22]M. M. Pratt, K. John, A. B. MacLean, S. Afework, D. H. Phillips, and M. C. Poirier, "Polycyclic aromatic hydrocarbon (PAH) exposure and DNA adduct semi-quantitation in archived human tissues." Int. J. Environ. Res. Public Health **8**, 2675–2691 (2011).

[23]N. A. Eaves, S. B. Dworkin, and M. J. Thomson, "The importance of reversibility in modeling soot nucleation and condensation processes," Proc. Comb. Inst. **35**, 1787–1794 (2015).

[24]A. Violi and S. Izvekov, "Soot primary particle formation from multiscale coarse-grained molecular dynamics simulation," Proc. Comb. Inst. **31**, 529–537 (2007).

[25]A. D'Anna, M. Sirignano, and J. Kent, "A model of particle nucleation in premixed ethylene flames," Combust. Flame **157**, 2106–2115 (2010).

[26]T. S. Totton, A. J. Misquitta, and M. Kraft, "A quantitative study of the clustering of polycyclic aromatic hydrocarbons at high temperatures," Phys. Chem. Chem. Phys. **14**, 4081–4094 (2012).

[27]A. Raj, M. Sander, V. Janardhanan, and M. Kraft, "A study on the coagulation of polycyclic aromatic hydrocarbon clusters to determine their collision efficiency," Combust. Flame **157**, 523–534 (2010).

[28]Q. Mao, A. C. T. van Duin, and K. H. Luo, "Formation of incipient soot particles from polycyclic aromatic hydrocarbons: A reaxff molecular dynamics study," Carbon **121**, 380–388 (2017).

[29]C. Saggese, S. Ferrario, J. Camacho, A. Cuoci, A. Frassoldati, E. Ranzi, H. Wang, and T. Faravelli, "Kinetic modeling of particle size distribution of soot in a premixed burner-stabilized stagnation ethylene flame," Combust. Flame **162**, 3356–3369 (2015).

[30]D. Aubagnac-Karkar, A. El Bakali, and P. Desgroux, "Soot particles inception and pah condensation modelling applied in a soot model utilizing a sectional method," Combust. Flame **189**, 190–206 (2018).

[31]T. S. Totton, D. Chakrabarti, A. J. Misquitta, M. Sander, D. J. Wales, and M. Kraft, "Modelling the internal structure of nascent soot particles," Combust. Flame **157**, 909–914 (2010).

[32]C. S. Wang, N. C. Bartelt, R. Ragan, and K. Thürmer, "Revealing the molecular structure of soot precursors," Carbon **129**, 537–542 (2018).

[33]H. Sabbah, L. Biennier, S. J. Klippenstein, I. R. Sims, and B. R. Rowe, "Exploring the role of pahs in the formation of soot: Pyrene dimerization," J. Phys. Chem. Lett. **1**, 2962–2967 (2010).

[34]E. M. Adkins, J. A. Giaccai, and J. H. Miller, "Computed electronic structure of polynuclear aromatic hydrocarbon agglomerates," Proc. Comb. Inst. **36**, 957–964 (2017).

[35]R. Scholz, R. Luschtinetz, G. Seifert, T. Jägeler-Hoheisel, C. Körner, K. Leo, and M. Rapacioli, "Quantifying charge transfer energies at donor–acceptor interfaces in small-molecule solar cells with constrained dftb and spectroscopic methods," J. Phys.: Condens. Matter **25**, 473201 (2013).

[36]A. A. M. H. M. Darghouth, M. E. Casida, W. Taouali, K. Alimi, M. P. Ljungberg, P. Koval, D. Sánchez-Portal, and D. Foerster, "Assessment of density-functional tight-binding ionization potentials and electron affinities of molecules of interest for organic solar cells against first-principles gw calculations," Computation **3**, 616–656 (2015).

[37]A. A. M. H. M. Darghouth, G. C. Correa, S. Juillard, M. E. Casida, A. Humeniuk, and R. Mitrić, "Davydov-type excitonic effects on the absorption spectra of parallel-stacked and herringbone aggregates of pentacene: Time-dependent density-functional theory and time-dependent density-functional tight binding," J. Chem. Phys. **149**, 134111 (2018).

[38]S. Zamith, M.-C. Ji, J.-M. L'Hermite, C. Joblin, L. Dontot, M. Rapacioli, and F. Spiegelman, "Thermal evaporation of pyrene clusters," J. Chem. Phys. **151**, 194303 (2019).

[39]L. Dontot, F. Spiegelman, and M. Rapacioli, "Structures and energetics of neutral and cationic pyrene clusters," J. Phys. Chem. A **123**, 9531–9543 (2019).

[40]M. Rapacioli, F. Spiegelman, A. Scemama, and A. Mirtschink, "Modeling charge resonance in cationic molecular clusters: Combining dft-tight binding with configuration interaction," J. Chem. Theory Comput. **7**, 44–55 (2011).

[41]P. B. Armentrout, K. M. Ervin, and M. T. Rodgers, "Statistical Rate Theory and Kinetic Energy-Resolved Ion Chemistry: Theory and Applications," J. Phys. Chem. A **112**, 10071–10085 (2008).

[42]M. T. Rodgers and P. B. Armentrout, "Statistical modeling of competitive threshold collision-induced dissociation," J. Chem. Phys. **109**, 1787–1800 (1998).

[43]P. B. Armentrout, "Statistical modeling of sequential collision-induced dissociation thresholds," J. Chem. Phys. **126**, 234302 (2007).

[44]F. Chirot, S. Zamith, P. Labastie, and J.-M. L'Hermite, "New device to study unimolecular cluster nucleation," Rev. Sci. Instrum. **77**, 063108 (2006).

[45]I. Braud, S. Zamith, and J.-M. L'Hermite, "A gas aggregation source for the production of heterogeneous molecular clusters," Rev. Sci. Instrum. **88**, 043102 (2017).

[46]A. I. S. Holm, H. Zettergren, H. A. B. Johansson, F. Seitz, S. Rosén, H. T. Schmidt, A. Ławicki, J. Rangama, P. Rousseau, M. Capron, R. Maisonny, L. Adoui, A. Méry, B. Manil, B. A. Huber, and H. Cederquist, "Ions colliding with cold polycyclic aromatic hydrocarbon clusters," Phys. Rev. Lett. **105**, 213401 (2010).

[47]P. Rousseau, A. Ławicki, A. Holm, M. Capron, R. Maisonny, S. Maclot, E. Lattouf, H. Johansson, F. Seitz, A. Méry, J. Rangama, H. Zettergren, S. Rosén, H. Schmidt, J.-Y.

Chesnel, A. Domaracka, B. Manil, L. Adoui, H. Cederquist, and B. Huber, "Low-energy ions interacting with anthracene molecules and clusters," Nuclear Instruments and Methods in Physics Research Section B: Beam Interactions with Materials and Atoms **279**, 140 – 143 (2012), proceedings of the Fifth International Conference on Elementary Processes in Atomic Systems Belgrade, Serbia, 21-25 June 2011.

[48]B. West, F. Useli-Bacchitta, H. Sabbah, V. Blanchet, A. Bodi, P. M. Mayer, and C. Joblin, "Photodissociation of pyrene cations: Structure and energetics from c16h10+ to c14+ and almost everything in between," J. Phys. Chem. A **118**, 7824–7831 (2014).

[49]D. Levine and R. B. Bernstein, Molecular Reaction Dynamics and Chemical Reactivity (Oxford University Press, 1987).

[50]P. B. Armentrout, "Kinetic energy dependence of ion–molecule reactions: guided ion beams and threshold measurements," International Journal of Mass Spectrometry Volume 200: The state of the field as we move into a new millenium, **200**, 219–241 (2000).

[51]P. B. Armentrout, "Mass spectrometry—Not just a structural tool: The use of guided ion beam tandem mass spectrometry to determine thermochemistry," Journal of the American Society for Mass Spectrometry **13**, 419–434 (2002).

[52]F. Muntean and P. B. Armentrout, "Guided ion beam study of collision-induced dissociation dynamics: integral and differential cross sections," The Journal of Chemical Physics **115**, 1213–1228 (2001).

[53]W. Forst, Unimolecular Reactions: A Concise Introduction (Cambridge University Press, 2003).

[54]A. I. S. Holm, H. a. B. Johansson, H. Cederquist, and H. Zettergren, "Dissociation and multiple ionization energies for five polycyclic aromatic hydrocarbon molecules," J. Chem. Phys. **134**, 044301 (2011).

[55]"Jmol: an open-source java viewer for chemical structures in 3d." `http://www.jmol.org/`.

[56]A. Cauchy, "Note sur divers théorèmes relatifs à la rectification des courbes et à la quadrature des surfaces," C.R. Acad. Sci. **13**, 1060–1065 (1841).

[57]T. Beitz, R. Laudien, H.-G. Löhmannsröben, and B. Kallies, "Ion Mobility Spectrometric Investigation of Aromatic Cations in the Gas Phase," The Journal of Physical Chemistry A **110**, 3514–3520 (2006).

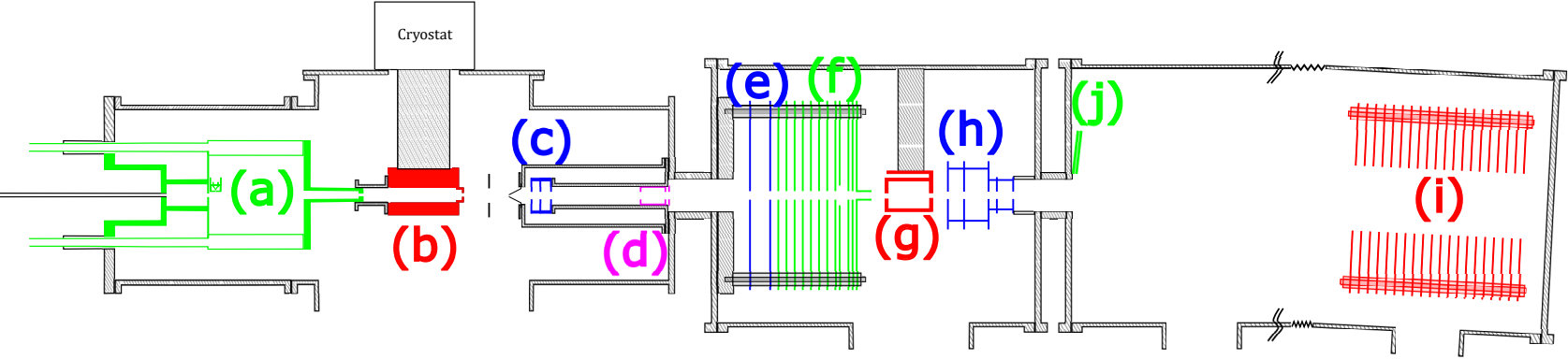
Cryostat
(a)
(b)
(c)
(d)
(e)
(f)
(g)
(h)
(j)
(i)

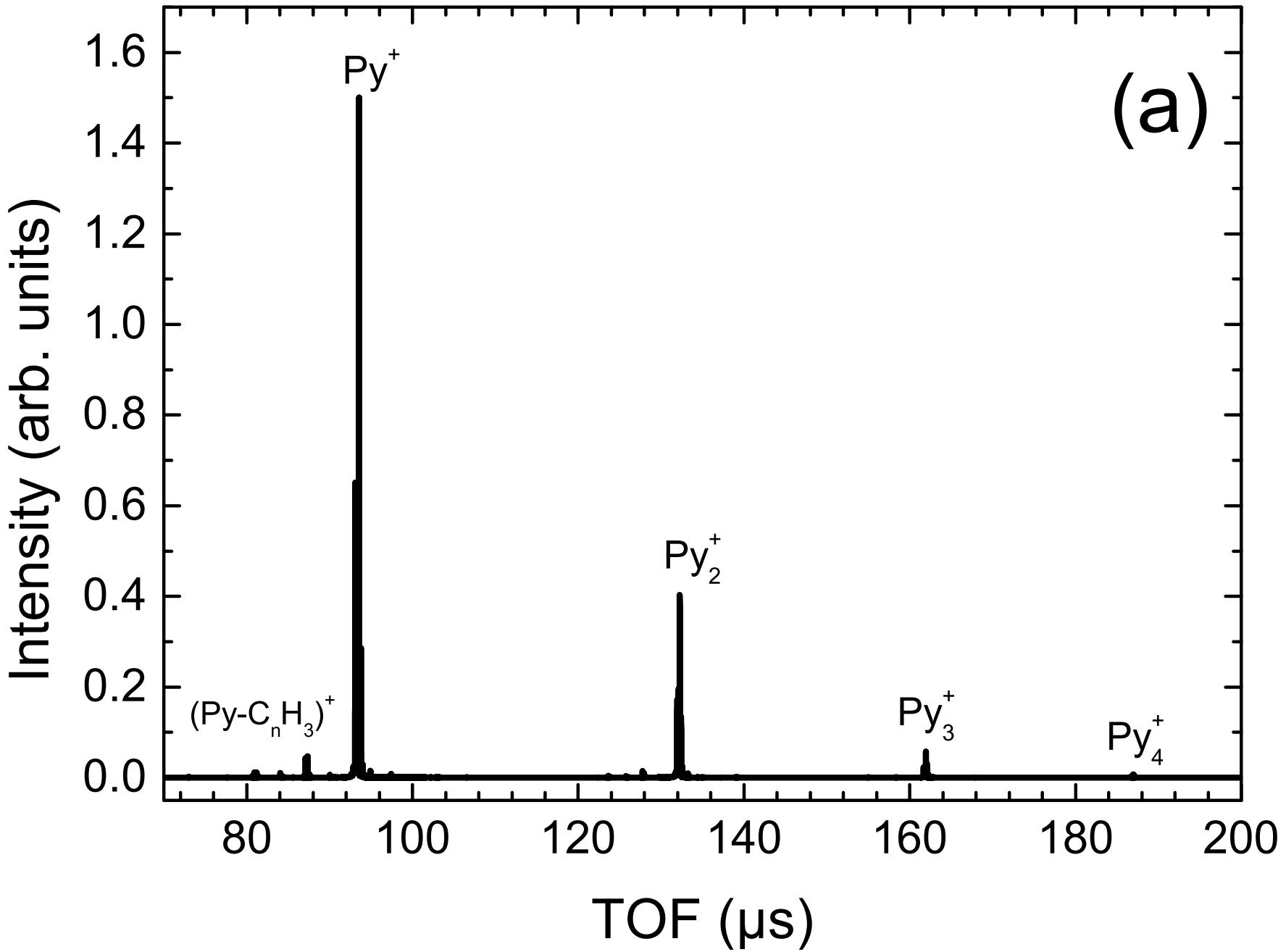
(a)
Intensity (arb. units)
TOF (μs)
1.6
1.4
1.2
1.0
0.8
0.6
0.4
0.2
0.0
80
100
120
140
160
180
200
Py+
Py2+
Py3+
Py4+
(Py-CnH3)+

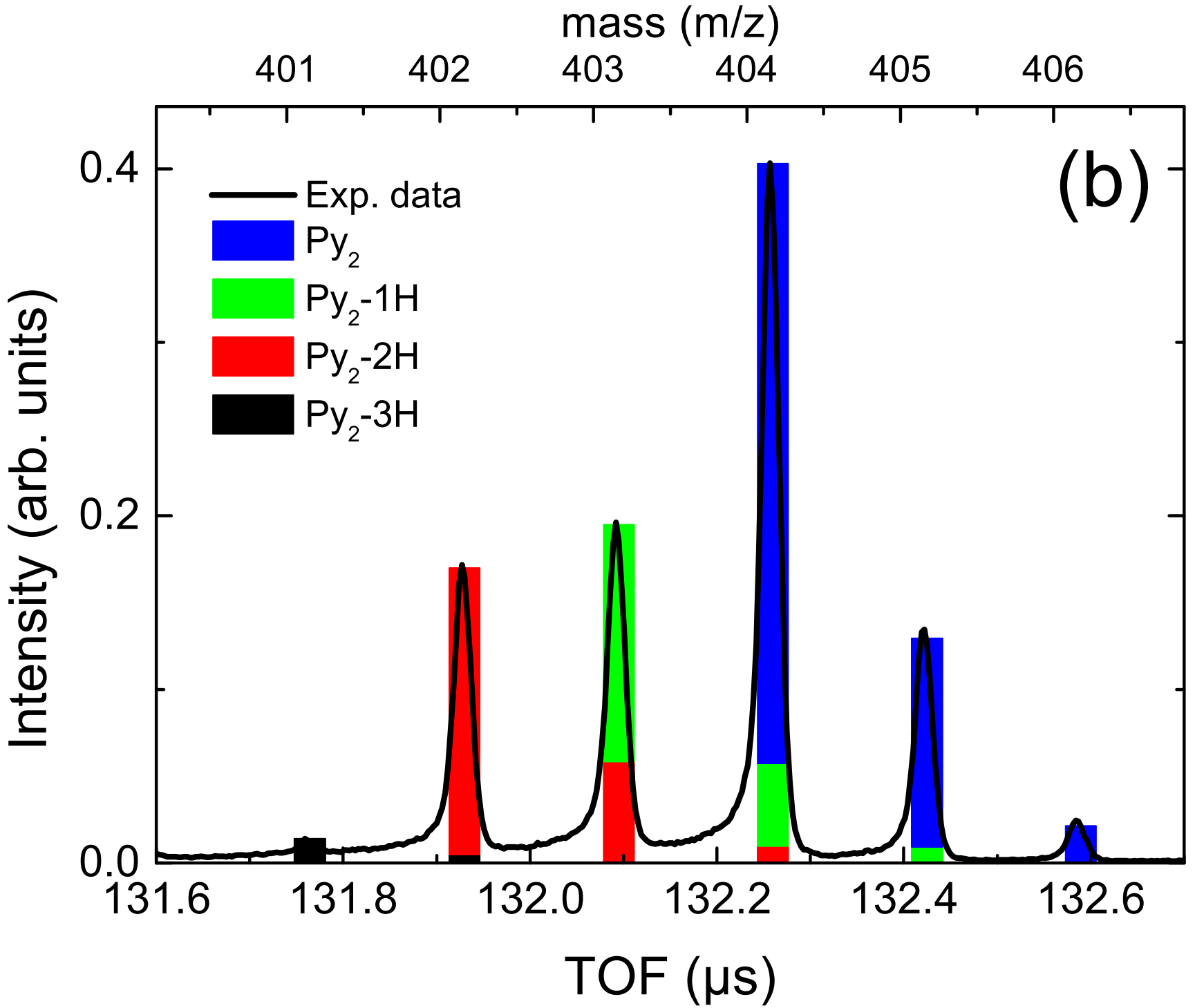
mass (m/z)
401
402
403
404
405
406
(b)
Exp. data
Py2
Py2-1H
Py2-2H
Py2-3H
Intensity (arb. units)
0.0
0.2
0.4
131.6
131.8
132.0
132.2
132.4
132.6
TOF (μs)

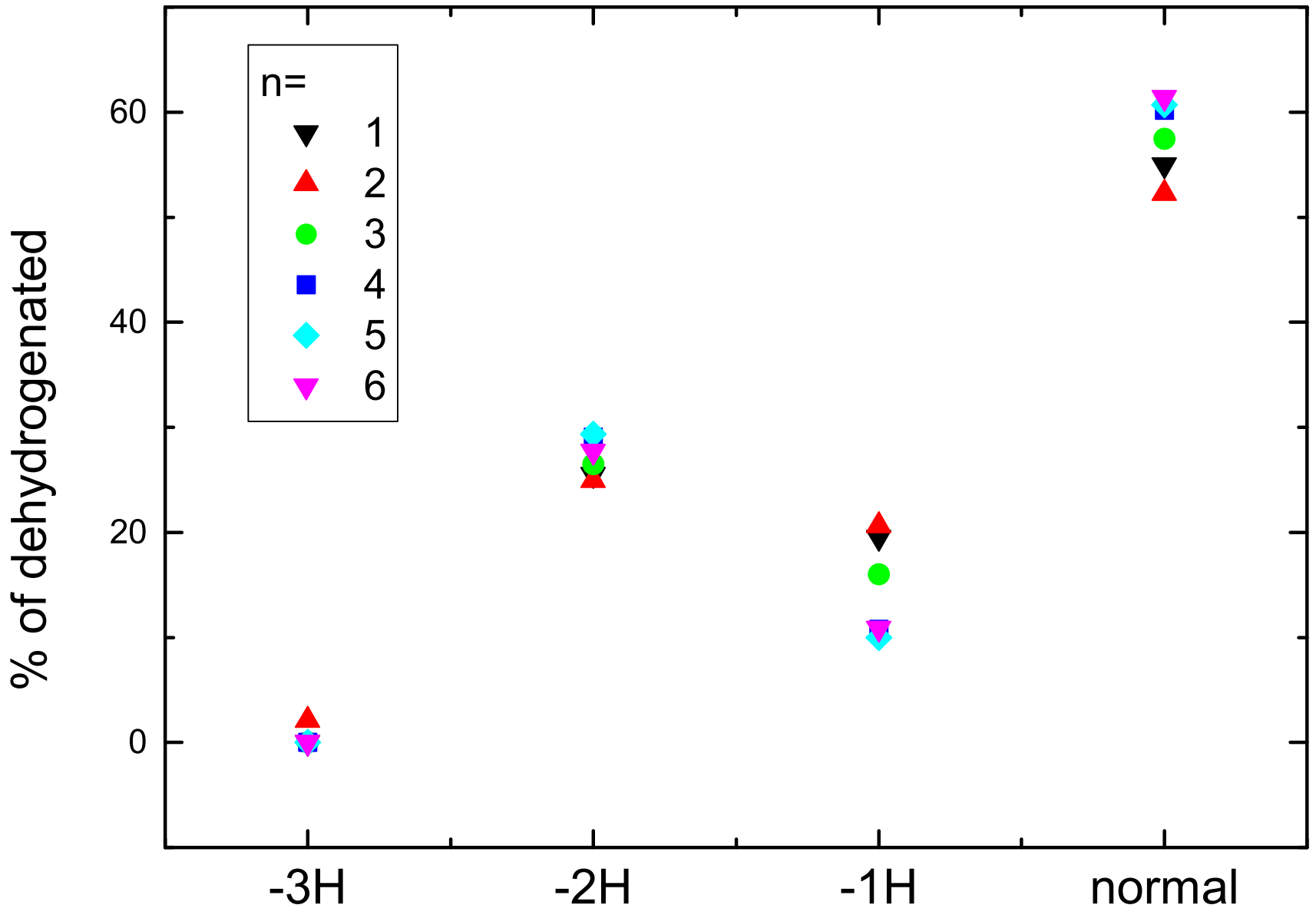
% of dehydrogenated
0
20
40
60
-3H
-2H
-1H
normal
n=
1
2
3
4
5
6

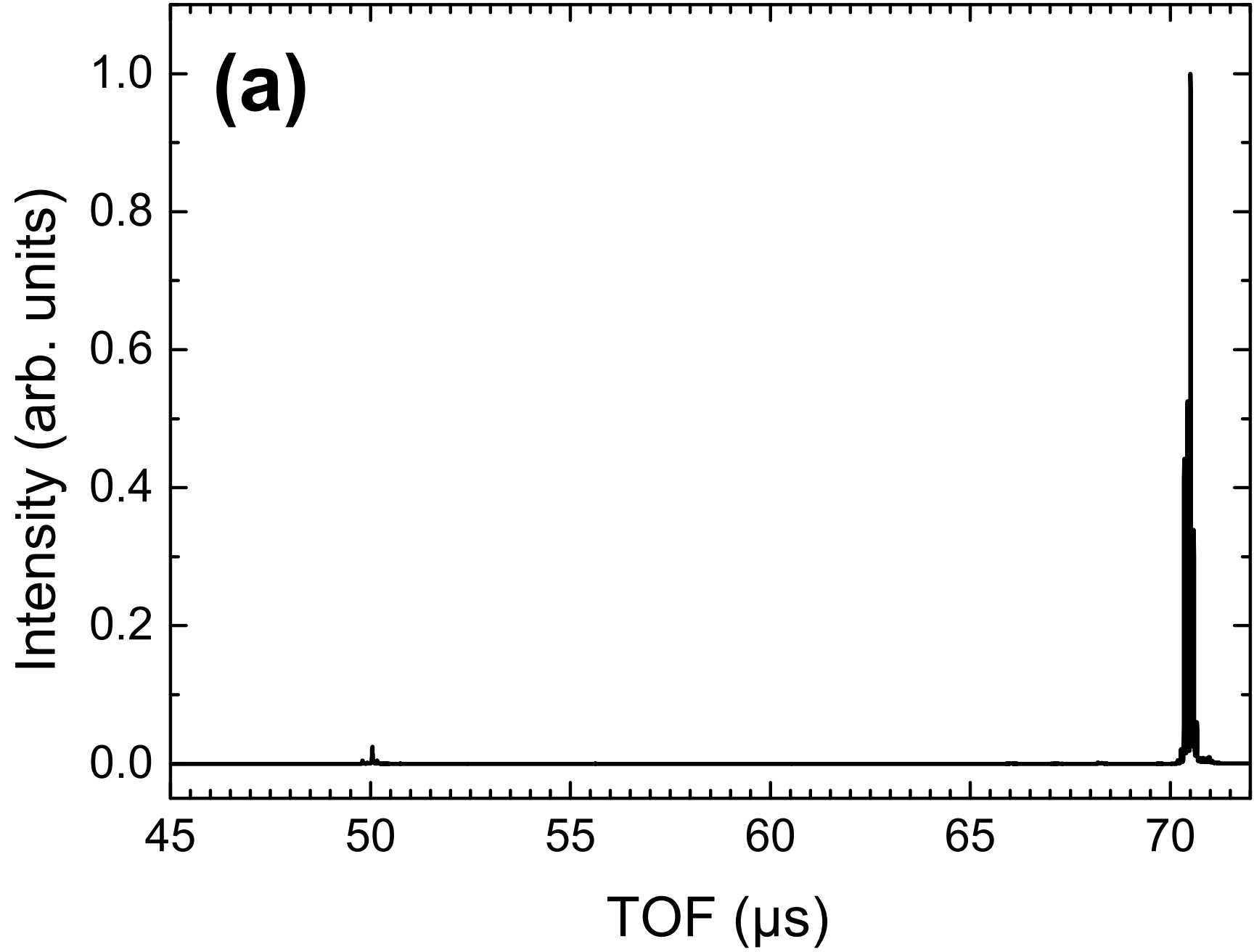
(a)
1.0
0.8
0.6
0.4
0.2
0.0
Intensity (arb. units)
45
50
55
60
65
70
TOF (μs)

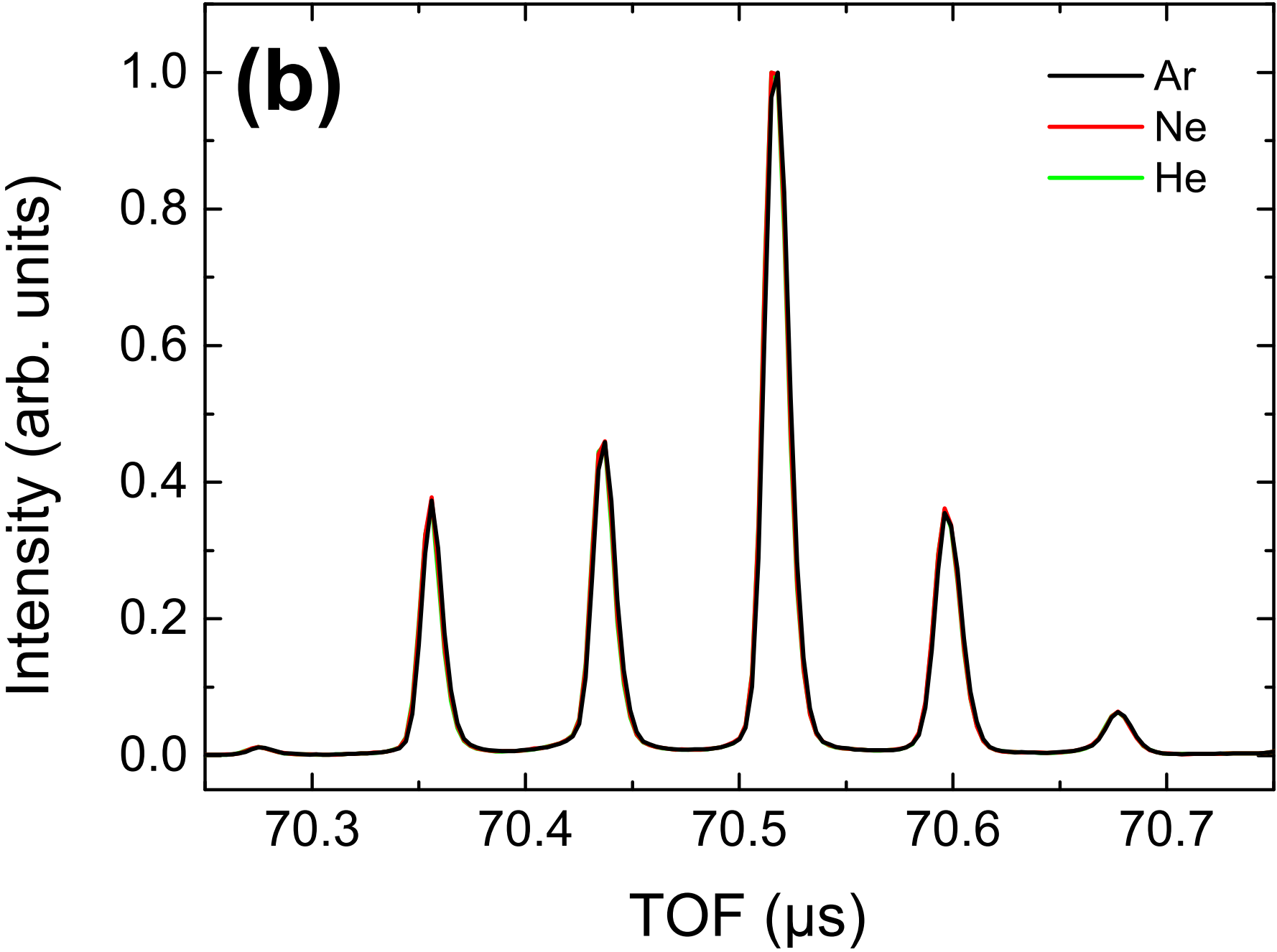
(b)
Ar
Ne
He
Intensity (arb. units)
1.0
0.8
0.6
0.4
0.2
0.0
70.3
70.4
70.5
70.6
70.7
TOF (μs)

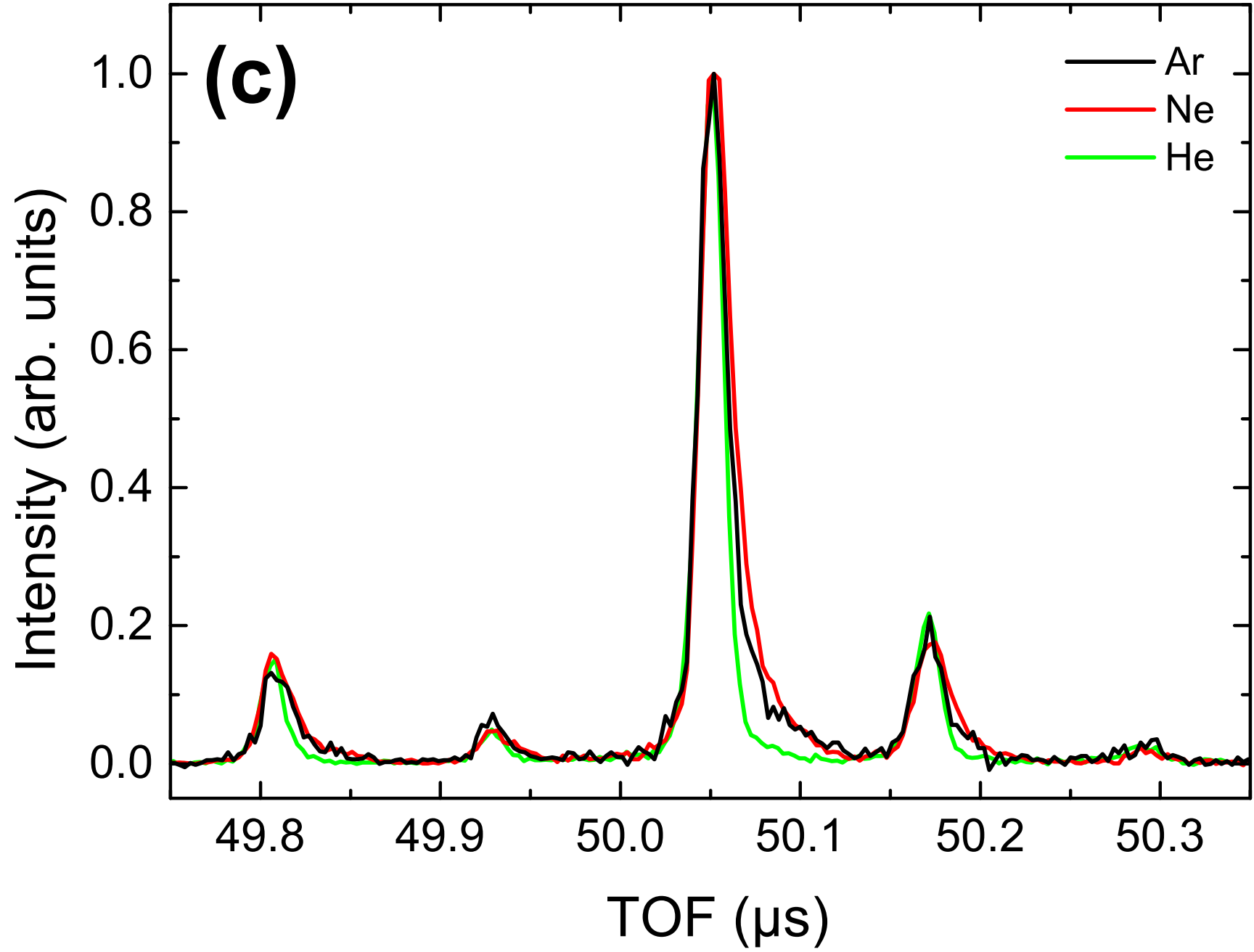
(c)
Ar
Ne
He
Intensity (arb. units)
1.0
0.8
0.6
0.4
0.2
0.0
49.8
49.9
50.0
50.1
50.2
50.3
TOF (μs)

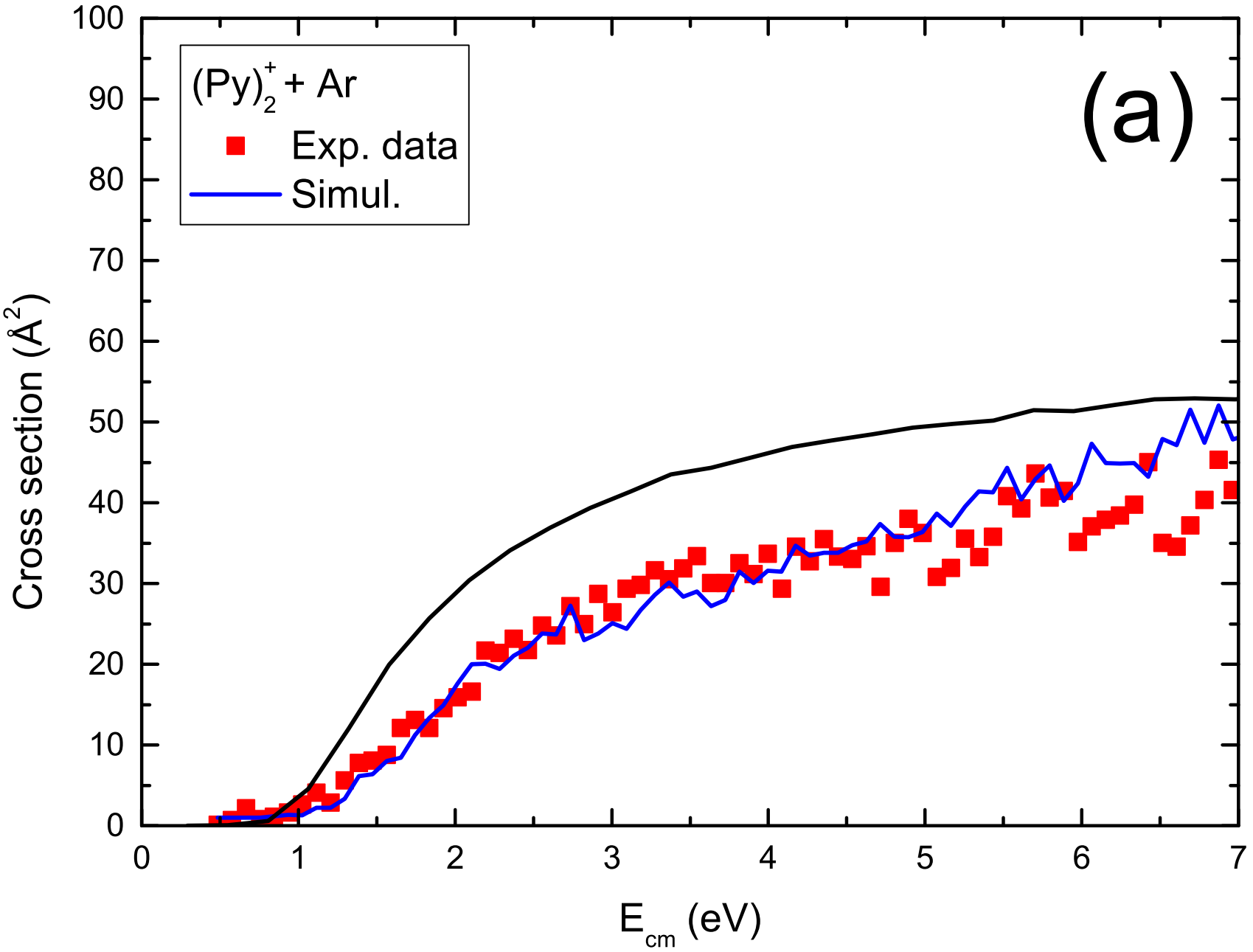
(Py)2+ + Ar
Exp. data
Simul.
(a)
Cross section (Å2)
Ecm (eV)
0
10
20
30
40
50
60
70
80
90
100
0
1
2
3
4
5
6
7

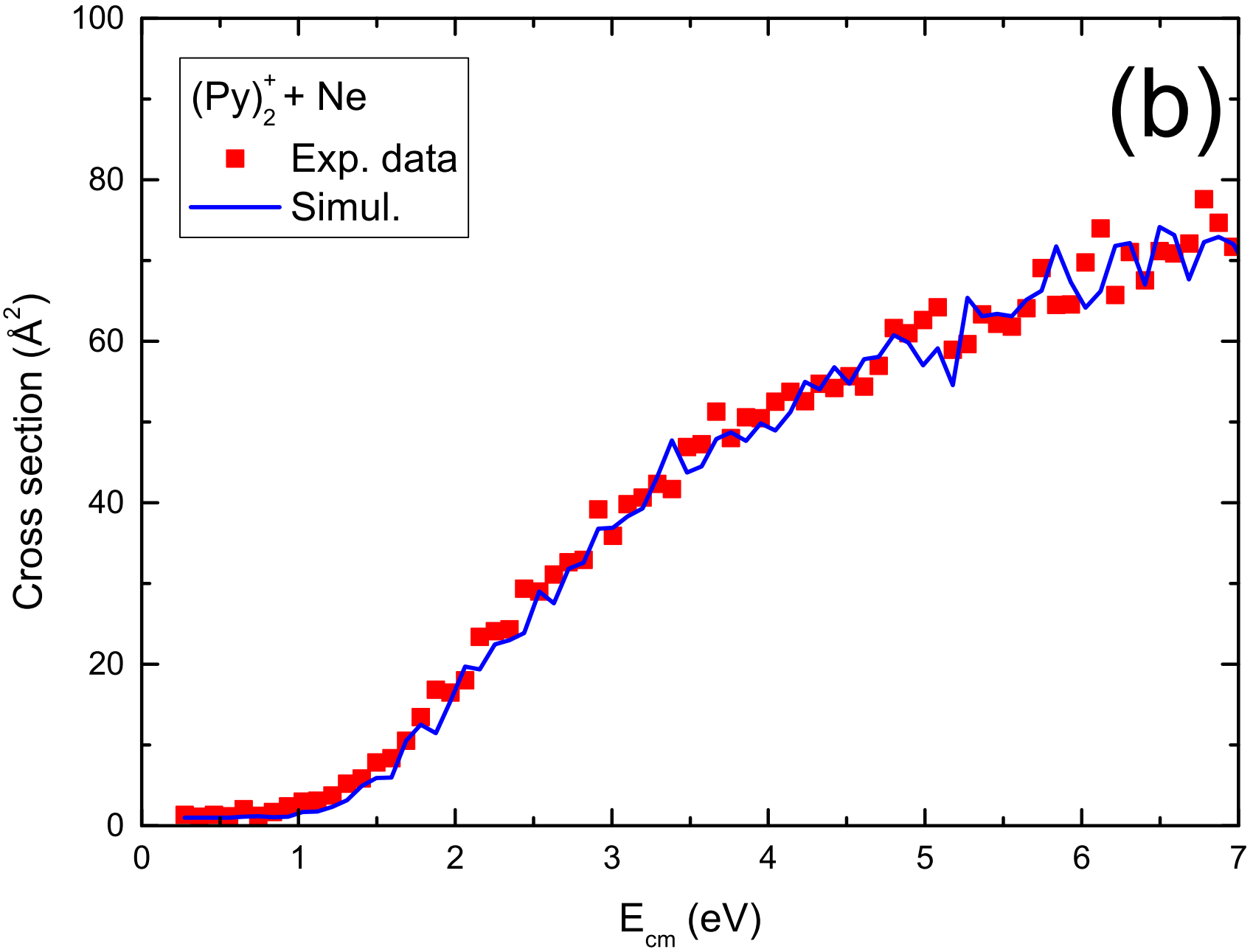
(b)
$(Py)_2^+$ + Ne
Exp. data
Simul.
Cross section (Å^2)
E_{cm} (eV)
0
20
40
60
80
100
0
1
2
3
4
5
6
7

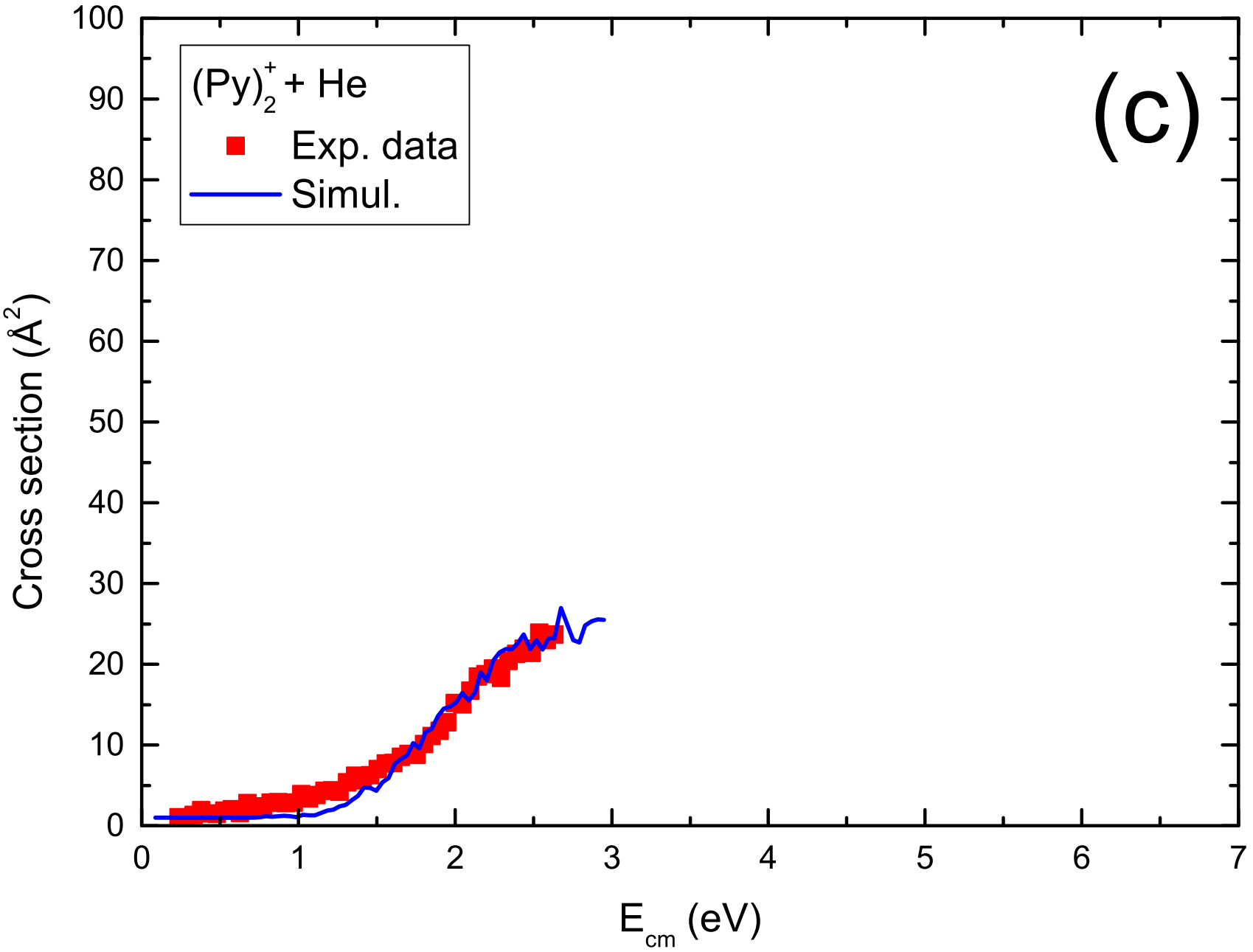
(Py)2+ + He
Exp. data
Simul.
(c)
Cross section (Å2)
Ecm (eV)
0
10
20
30
40
50
60
70
80
90
100
0
1
2
3
4
5
6
7

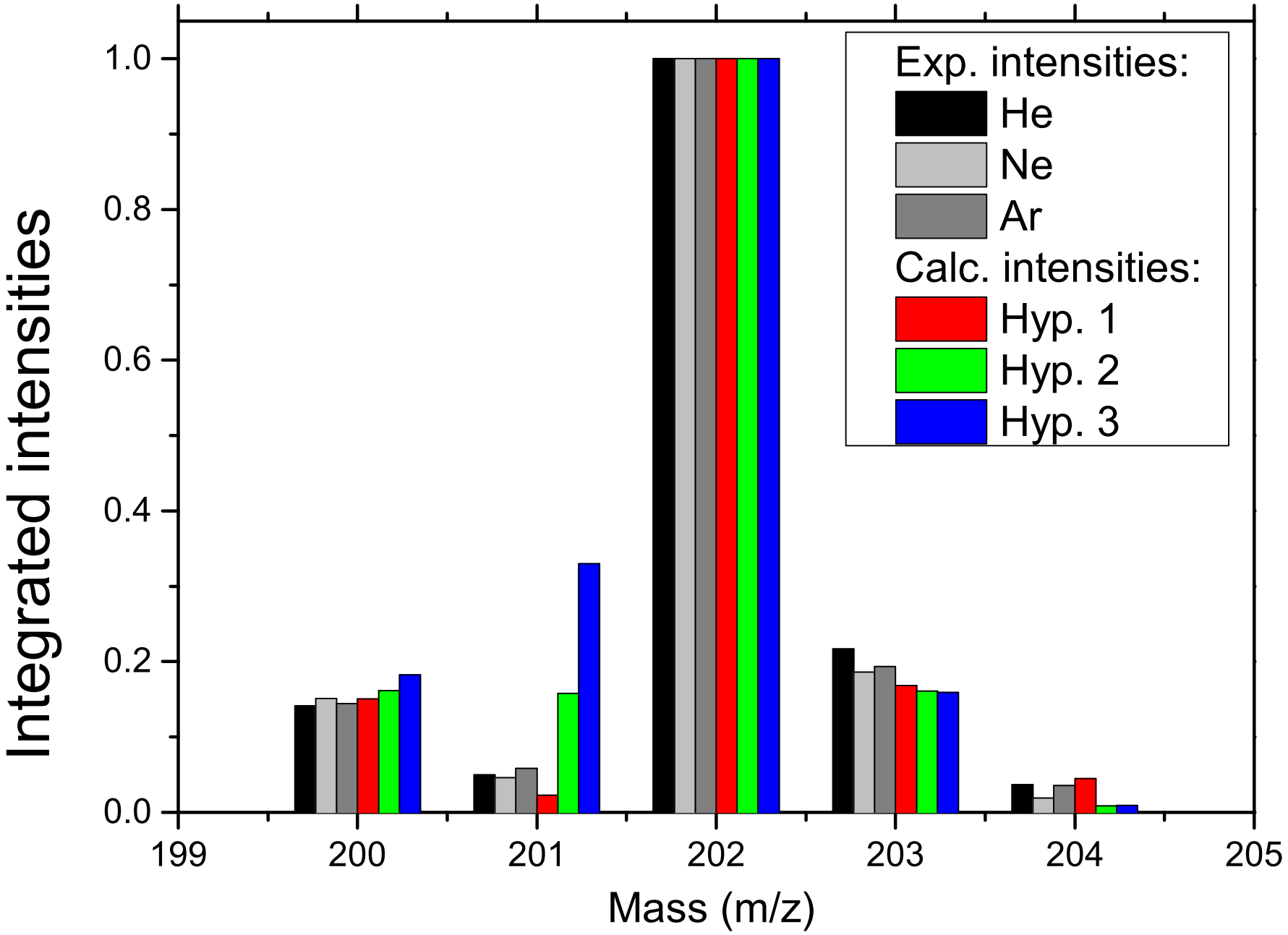
Integrated intensities
1.0
0.8
0.6
0.4
0.2
0.0
199
200
201
202
203
204
205
Mass (m/z)
Exp. intensities:
He
Ne
Ar
Calc. intensities:
Hyp. 1
Hyp. 2
Hyp. 3

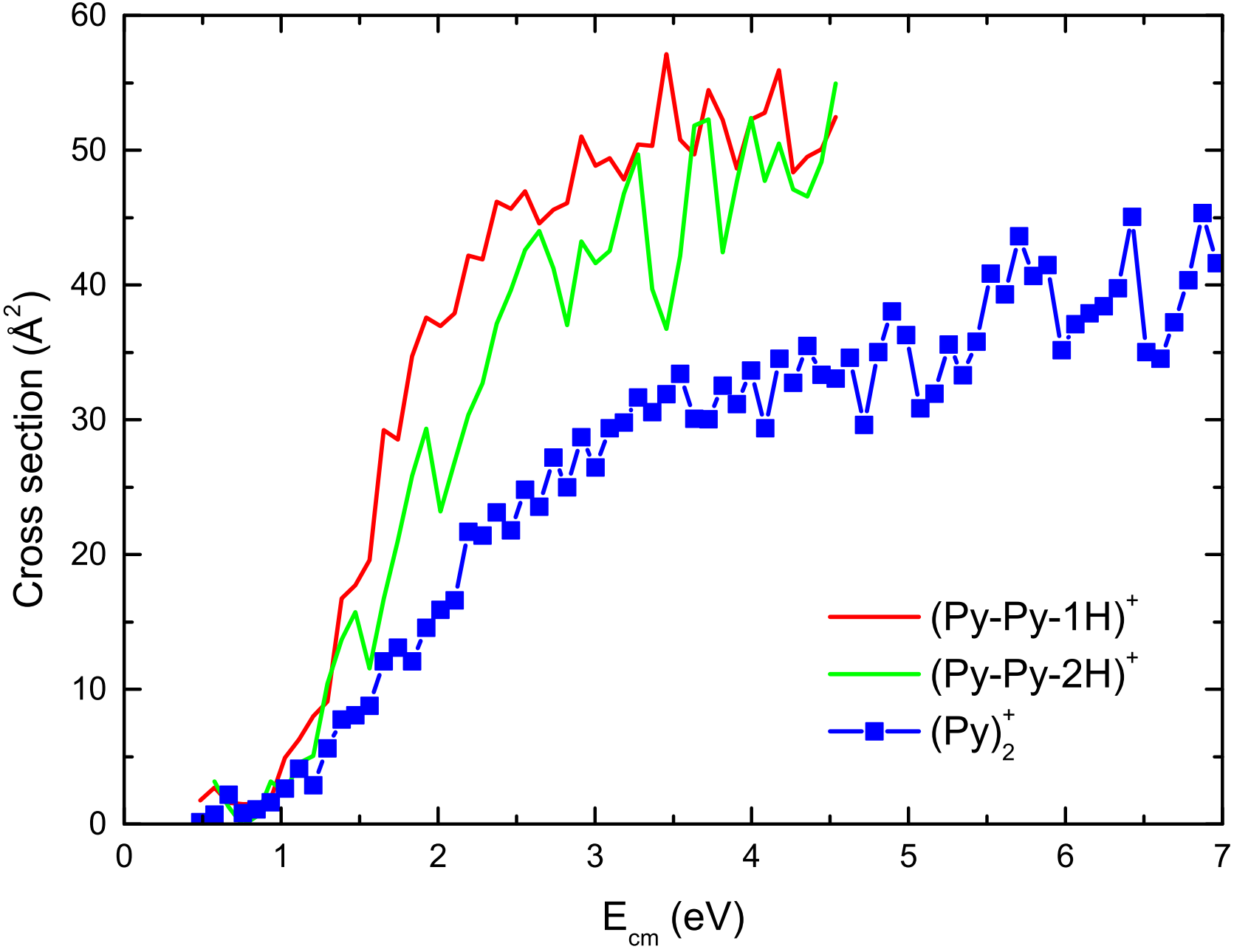
Cross section (Å^2)
E_{cm} (eV)
(Py-Py-1H)$^+$
(Py-Py-2H)$^+$
(Py)$_2^+$
0
10
20
30
40
50
60
0
1
2
3
4
5
6
7

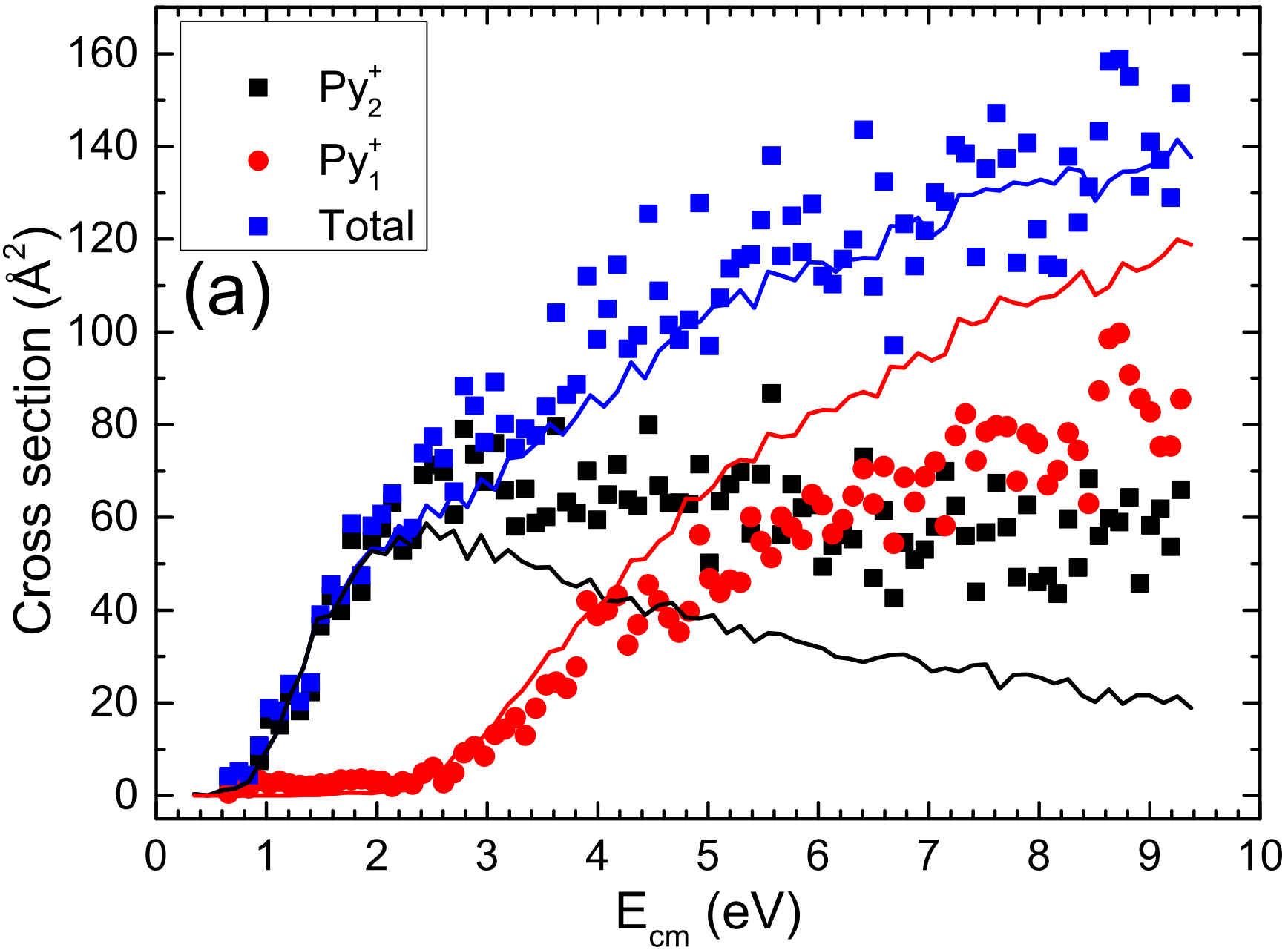
Py2+
Py1+
Total
(a)
Cross section (Å2)
Ecm (eV)
0
20
40
60
80
100
120
140
160
0
1
2
3
4
5
6
7
8
9
10

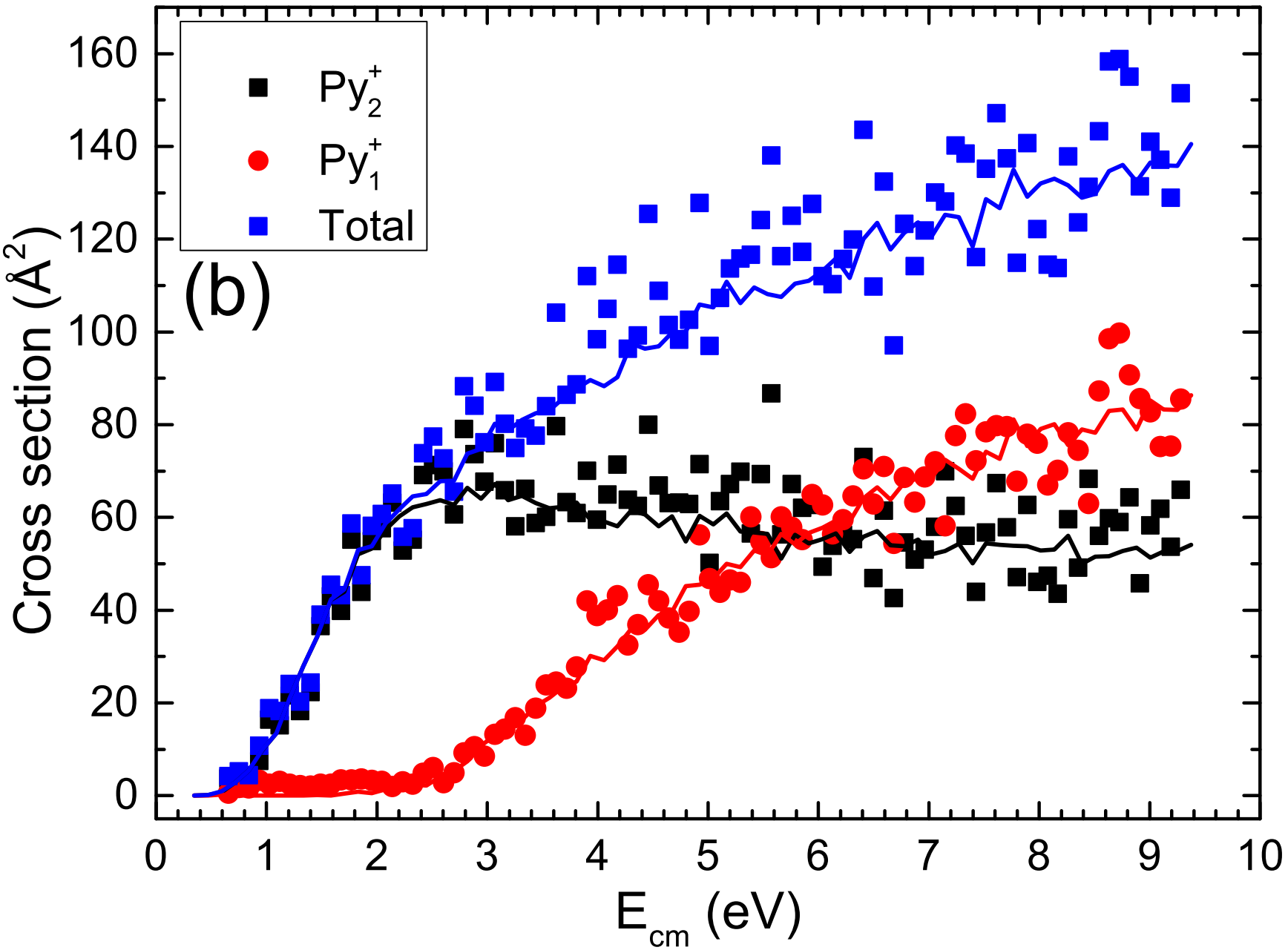
(b)
Py_2^+
Py_1^+
Total
Cross section (Å^2)
E_{cm} (eV)
0
20
40
60
80
100
120
140
160
0
1
2
3
4
5
6
7
8
9
10

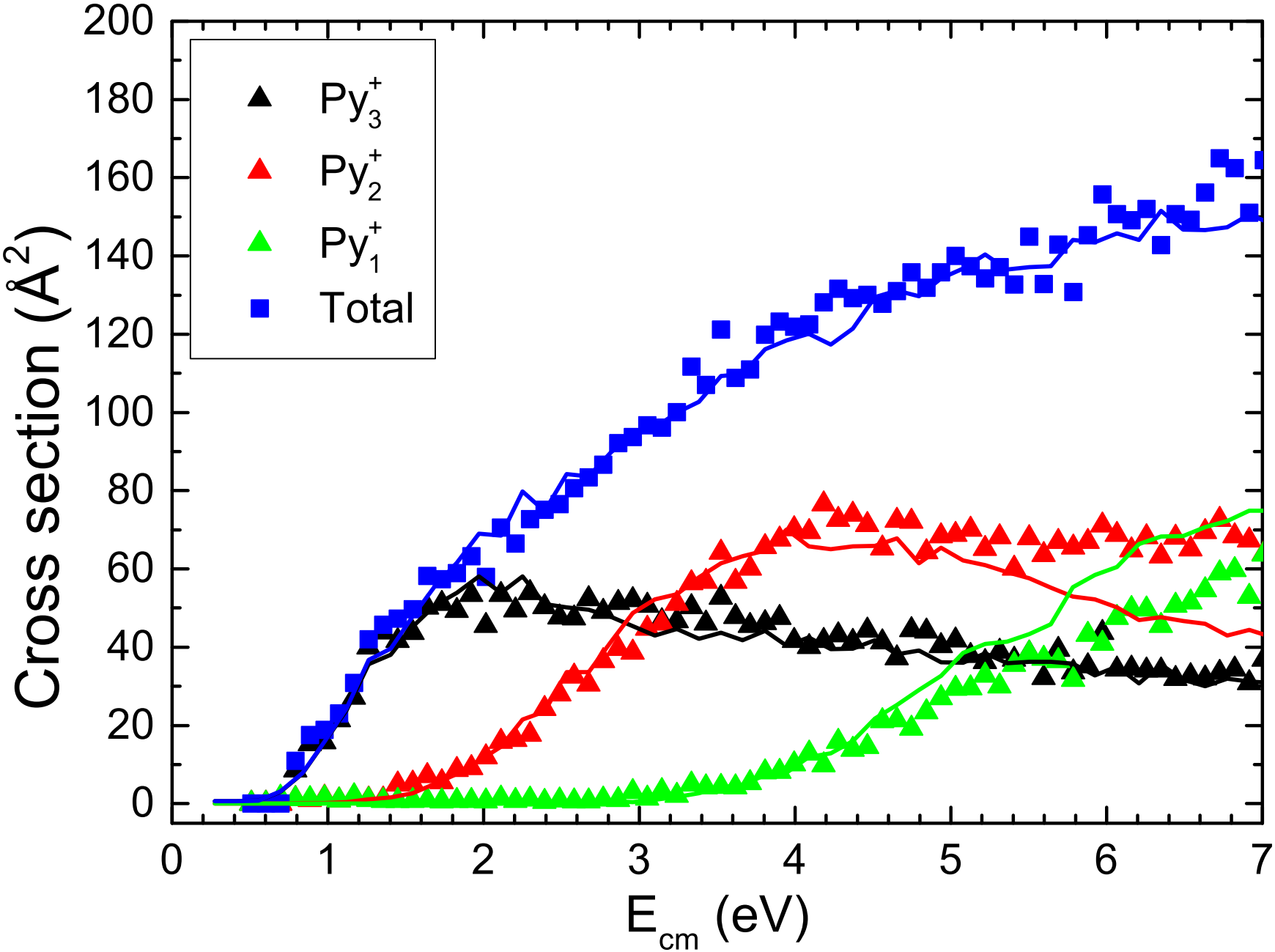
Cross section (Å^2)
E_{cm} (eV)
Py_3^+
Py_2^+
Py_1^+
Total
0
20
40
60
80
100
120
140
160
180
200
0
1
2
3
4
5
6
7

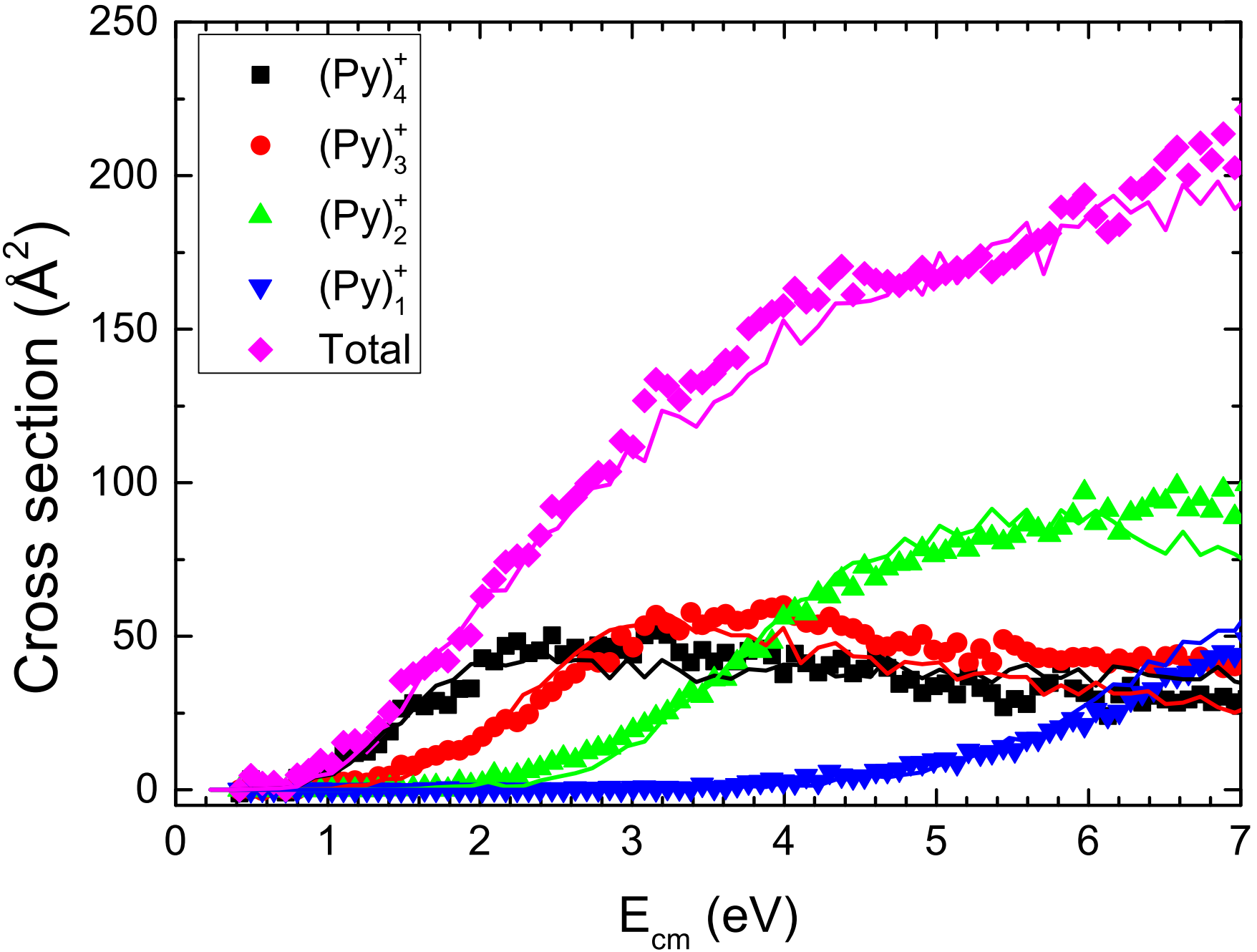
250
200
150
100
50
0
0
1
2
3
4
5
6
7
Cross section (Å^2)
E_{cm} (eV)
$(Py)_4^+$
$(Py)_3^+$
$(Py)_2^+$
$(Py)_1^+$
Total

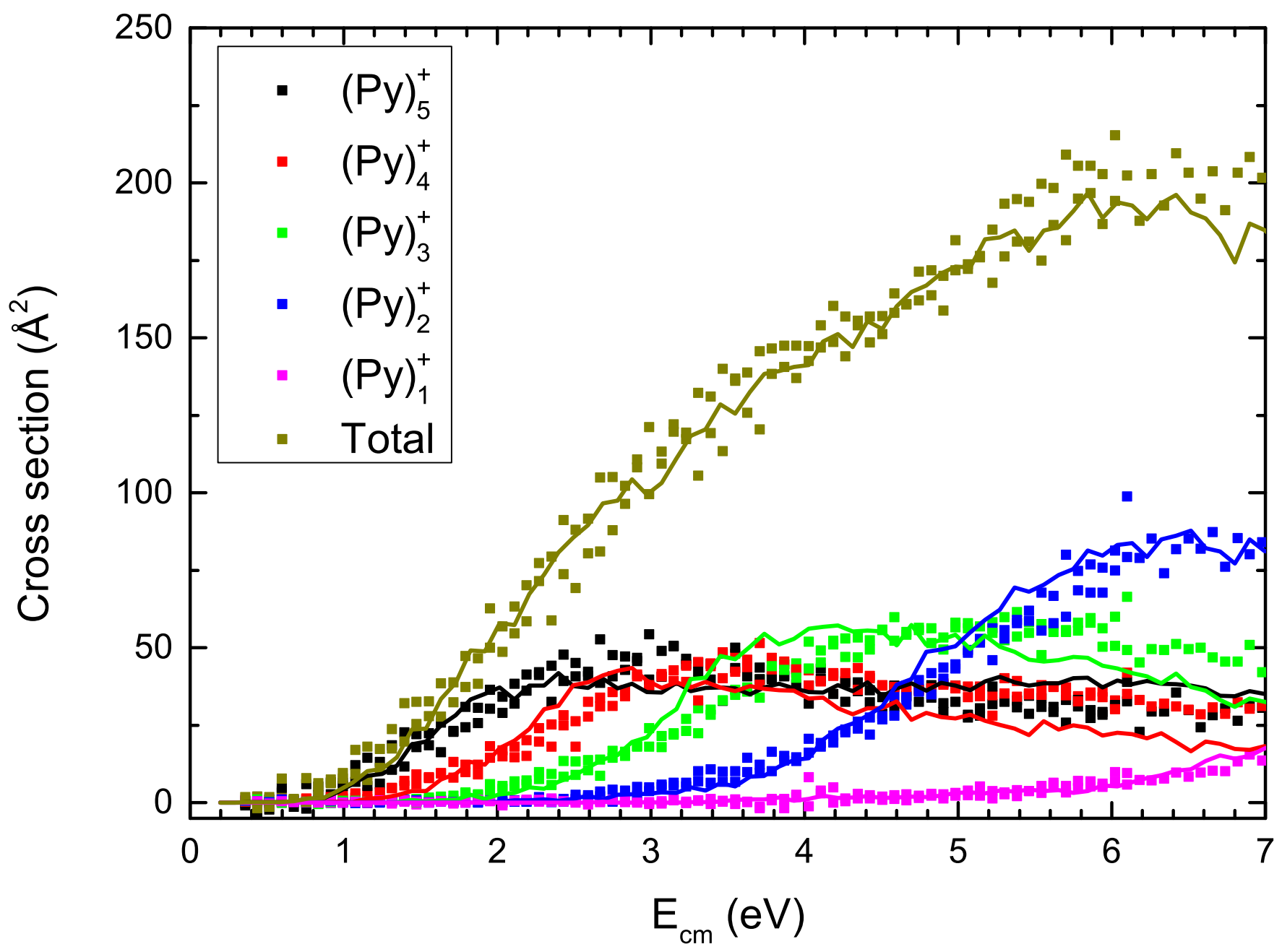
250
200
150
100
50
0
0
1
2
3
4
5
6
7
Cross section (Å^2)
E_{cm} (eV)
$(Py)_5^+$
$(Py)_4^+$
$(Py)_3^+$
$(Py)_2^+$
$(Py)_1^+$
Total

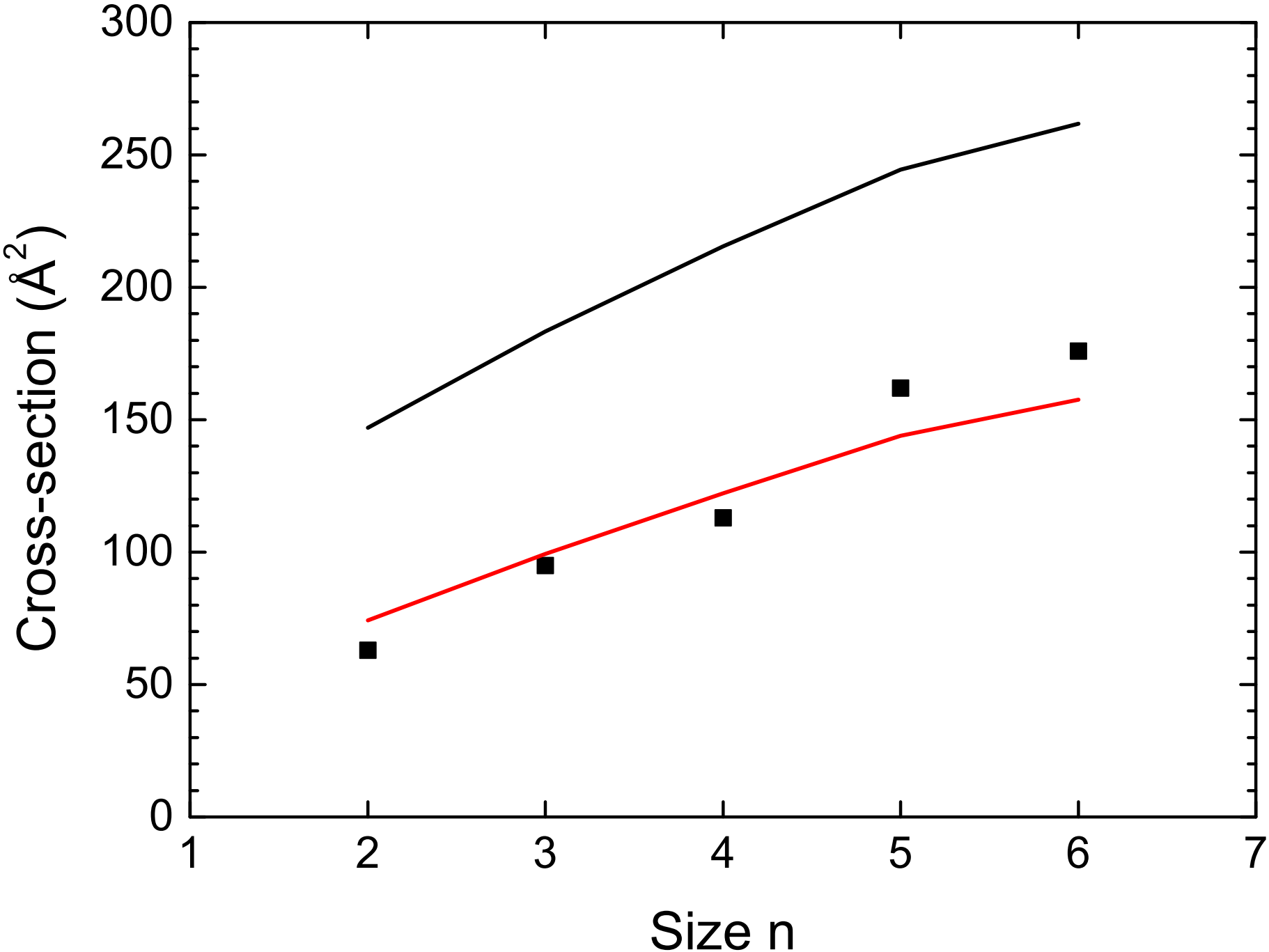
300
250
200
150
100
50
0
Cross-section (Å^2)
1
2
3
4
5
6
7
Size n

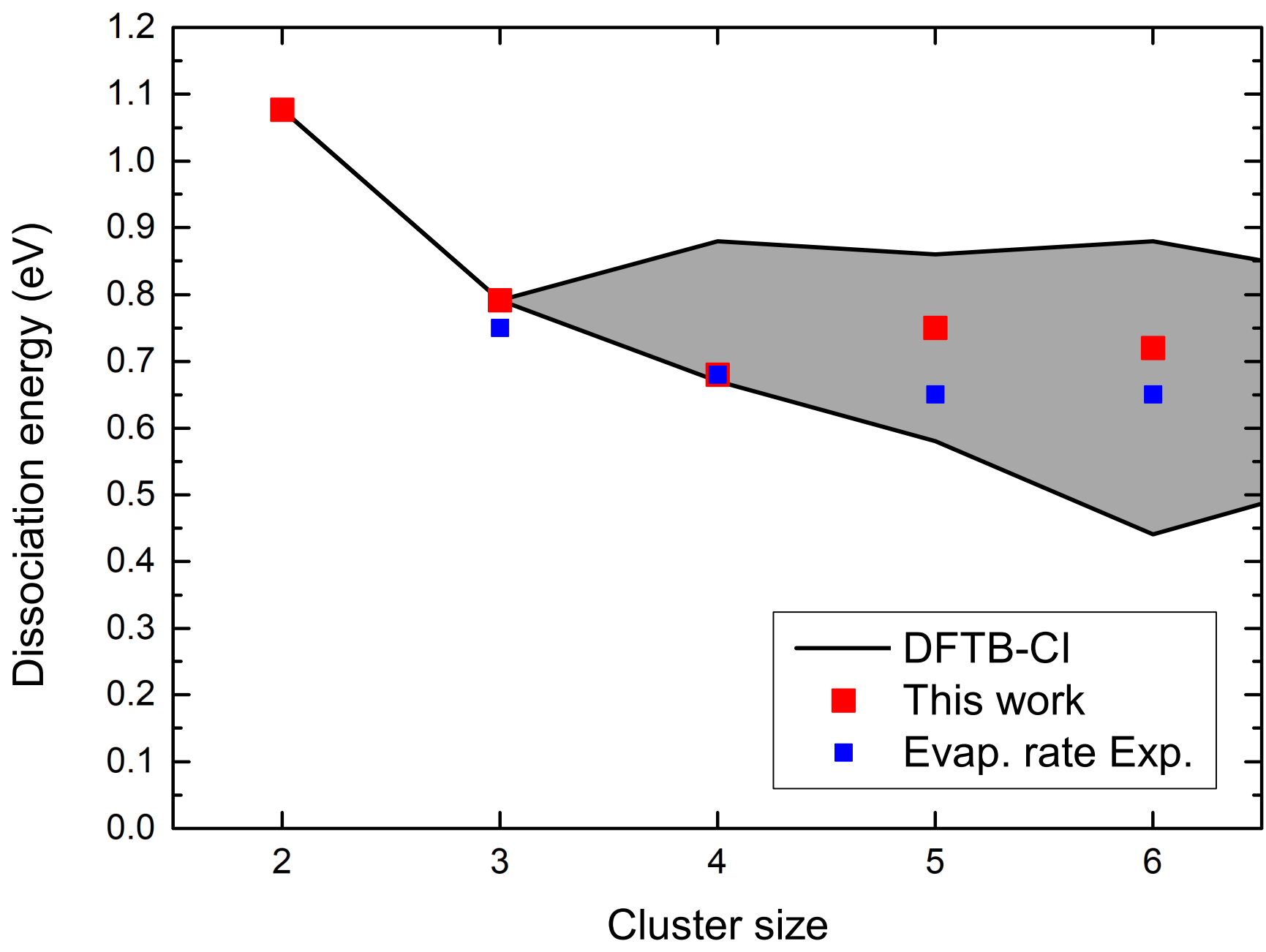
Dissociation energy (eV)
1.2
1.1
1.0
0.9
0.8
0.7
0.6
0.5
0.4
0.3
0.2
0.1
0.0
2
3
4
5
6
Cluster size
DFTB-CI
This work
Evap. rate Exp.